UNIVERSITY OF BIRMINGHAM

EM SENSOR MEASUREMENTS OF DEGRADATION IN STEELS

MSc REPORT

HANSEN ZHOU

Metallurgy and Materials Science

AUG 2014

Supervisors: Prof C.L. Davis and Dr M. Strangwood

Word count: 15763

Abstract

The limitation of power plant steel components designed for high temperature operation is mainly related to microstructural degradation and associated creep damage. Electromagnetic (EM) sensors can be used to detect phase transformation during processing, microstructural alterations due to heat treatment or in-service thermal exposure and the presence of cracks in steel. EM sensors primarily detect changes in the near surface microstructure of steels, due to changes in relative permeability and/or electrical resistivity, and are therefore sensitive to the components surface condition. During oxidation of carbon steel three different forms of iron oxide can form (FeO, Fe_2O_3 and Fe_3O_4), one of which (Fe_3O_4, magnetite) is ferromagnetic, whilst the other two forms are paramagnetic. During oxidation of alloyed steel complex spinel type oxide films can also form. The relationship between the EM signal and the presence of oxide films, generated by heat treatment, for power plant steel grades T22 and P91 and plain carbon steel are discussed in this report. The samples were heat treated for up to 75 hours at 650 and 700 ℃. It has been found that oxide films with different thicknesses were generated and these oxide films affected the EM signals. A comparison between EM signals for these samples with oxide films compared to an equivalent lift off (i.e. distance between the EM sensor and un-oxidised sample surface) was also made. It has been found that the oxide films behave predominantly as an equivalent lift off in terms of their effect on the EM signals. Observation of the oxide films showed the presence of different oxide types with significant porosity also being present. The results indicate that the effect of any magnetite present in the oxide on the EM signal is less than the experimental error in the measurements.

Acknowledgements

I want to give my sincere thanks to my supervisors, Prof C.L. Davis, who gave me encouragements and help during my master and undergraduate study, and Dr Martin Strangwood, who gave me opportunities to face challenges and helped me with many little things in my academic work.

Acknowledgements are given to my mentor, Mr Lei Zhou, for his encouragements and help with my academic research study, and even my life.

Thanks are also given to Dr X.J. Hao, who gave me a great help in my Masters project.

Also, I would like to thank Dr Jun Liu who helped me with sample preparation.

Finally, I would like to give my thanks to my Mum and Dad, who gave me great support when some disasters come up to myself, all the members in our research group, and some postgraduates in the department, for their support and encouragements over the past year.

Lists of Contents

Lists of Figures

Lists of Tables

1. Introduction

As there is no danger of running out of coal in the near future, steam based power plants will continue to play a role in energy generation for several decades. It has been reported that more than half of the UK electricity generation is dependent on steam power plants [1]. In order to decrease the CO_2 emissions, an increase in plant efficiency from 35% to 50% is desired, this can be achieved by increasing the operating temperature and pressure up to 600-650 ℃ and 30MPa [2]. Energy efficiency is extremely important in counties such as China and India as they have thousands of coal-fired power plants in their grid.

Ferritic and martensitic steels do not meet the requirements for mechanical properties, such as creep strength and fatigue life, at very high temperatures and pressures [3]. The limiting operation temperature of these steels is up to around 620 ℃ due to their creep, oxidation and hot corrosion behaviour [3]. The materials designed for boiler tubes need to be capable of being processed to shape and/or welded, as well as being creep resistant and corrosion (steam side oxidation) resistant [3]. Austenitic steels can be used in the higher temperature regions in conventional power plants as their better corrosion and oxidation resistance allows higher temperature operation, leading to higher efficiency [3]. The consequence of failure of a component in-service can be expensive and unpredictable. Many cases of engineering disaster result in the loss of property and life. For boiler or power plant components, particular attention is required to avoid accidents taking place [2, 3].

Oxide films will form on steels during high temperature exposure, such as for power generation components that can experience temperatures of >600 ℃. The chemical composition and properties of the oxide films that form are influenced by the environment (e.g. temperature, presence of steam or other chemicals) and the type of steel [4]. These oxide films can be protective and thus increase the life time of the component, for example by loss of material affecting the structural integrity of the component.

Multi-frequency electromagnetic (EM) sensors can be used to monitor material (microstructural) alterations by a change in sensor signal response. Previously, X.J. Hao et al. have shown that a multi-frequency EM sensor could monitor the ferrite-

austenite transformation during cooling and detect the presence of a decarburized layer in steel [5, 6]. L. Zhou et al. have shown that steels with different microstructures, due to differences in carbon content, give different EM readings [7]. The effects of the key microstructure parameters on the EM sensor readings are subjected to on-going study. The EM sensor signal is affected by the surface condition of the steel, as evidenced by Hao et al. work on decarburisation [5]. It is expected that the presence of an oxide film will also affect the EM signal either through a change in lift off (distance of the sensor to the steel surface) and / or because of the ferromagnetic properties of magnetite (one of the oxides that can form on steel). This means that any degradation in power plant steel microstructure, due to thermal exposure, may not be successfully detected by an EM sensor if the presence of an oxide film modifies the sensor signal. Therefore the influence of oxide films on the EM sensor signal needs to be determined.

Aim of the project

The aim of the project is to study the effects of steel oxidation on the EM sensor signal, by taking into account the type (paramagnetic or ferromagnetic), porosity and thickness of the oxide film, for plain carbon steel, and T22 and P91 grades (commonly used in power plants). Experimental studies on samples heat treated to generate different thickness oxide films is required to understand the effect of an oxide film on the EM sensor signal.

2. Literature review

2.1. General Principles of Oxidation

2.1.1. Initial oxidation reaction in air and water vapour

An oxidation reaction on steam plant steel components will take place in dry and wet conditions at the elevated temperatures experienced. The term 'dry' refers to when the oxidation reaction occurs without aqueous solution or water present; the term of 'wet' refers to conditions when an aqueous solution is involved in the reaction mechanism [8]. Considering oxidation taking place under 'dry' conditions, the general chemical equation is shown below:

$$aMe + \frac{b}{2}O_2 \rightarrow Me_aO_b \qquad \text{(Eq. 2.1)}$$

Where Me is the metal, O_2 is oxygen and a,b are parameters relating to the type of oxide that form.

There are three kinds of oxide films that form on iron; magnetite, hematite and wüstite. FeO (wustite), where a=1 and b=1; Fe_3O_4 (magnetite), where a=3 and b=4; Fe_2O_3 (hematite), where a=2 and b=3. In addition mixed oxides (e.g. $Fe_{1.2}Cr_{0.8}O_3$ and $Mn_{1.5}Cr_{1.5}O_4$ [9]) can form on alloyed steels containing Cr. It is important to know the relative permeability and electrical conductivity of the oxide films as these parameters affect the EM sensor system. These properties differ from the steel properties (ferritic or martensitic) and are shown in Table 2.1.

Table 2.1: Properties of iron oxide (www.Matweb.com)*

	FeO	Fe_2O_3	Fe_3O_4
Relative permeability	1.0008	1.0012	200-240
Conductivity (S/m)	6E+4	2.1E+5	2E+5

**(No data for mixed oxides has been reported)*

The 'dry' reaction first takes place with the adsorption of gas on the clean metal surface. This adsorption can be divided into two parts, chemisorption and

physisorption. Chemisorption involves oxygen forming a chemical bond with atoms on the surface by the transfer of electrons. Physisorption involves Van der Waals forces which bond the gases to the surface [10]. Oxide nuclei initially form between the dissolved oxygen and metal, then a continuous reaction occurs to form a thin oxide film. In order to continue the oxidation process, two mechanisms can take place, one is metal ions diffuse outward through the oxide to the oxide-gas interface and react to form an outer layer, or oxygen ions diffuse through the metal-oxide interface and react to form an inner layer. The different rates of reaction for these mechanisms can lead to a spallation phenomenon, which will be introduced in section 2.1.2 [11, 12]

For power plant steels the oxide that forms in the dry reaction depends on the concentration of the chromium present. When chromium is present in the alloy, then hematite and chromium rich oxides will both form on the surface. With an increasing amount of chromium, the Fe^{2+} ions are blocked by the $FeCr_2O_4$ inter-layer so the wüstite (FeO) layer will be thinner [11]. When designing an alloy composition to resist oxidation the Ellingham diagram can be used to compare the stability of the different oxides [10]. Figure 2.1 shows the Ellingham diagram and stabilities for different oxidation reactions. Ellingham diagram shows the thermodynamic feasibility of a reaction relate to Gibbs free energy (ΔG) [10, 11]. The higher the reaction line on the diagram, the less stable the oxide is [10, 11]. Therefore, it can be seen from the diagram that Cr, Si and Al are all low on the diagram, below iron oxide, and hence they can form protective oxides.

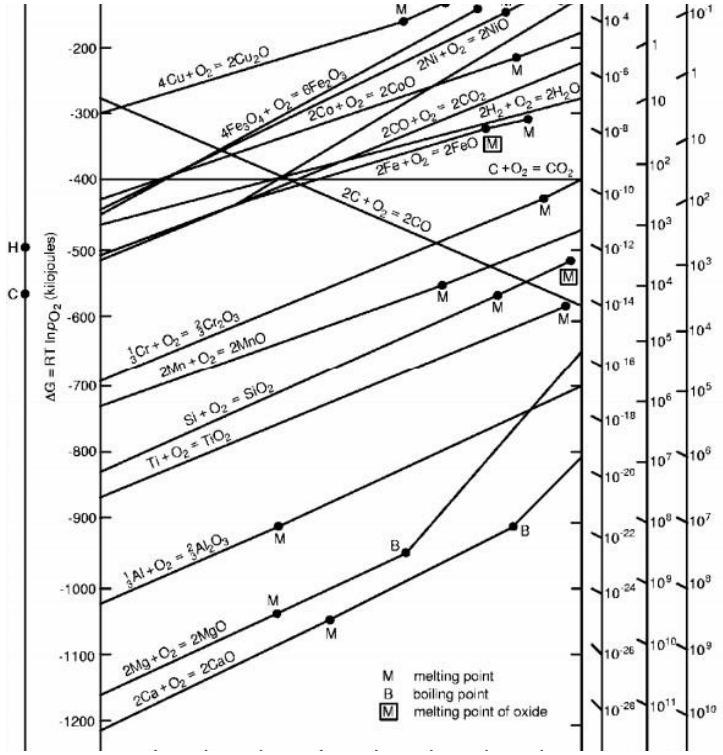

Figure 2.1: An Ellingham diagram displaying common oxides [13]

In the 'wet' reaction, which had been researched by Fujii and Meussner in 1964 [14], the reactions that occur for a Cr-alloyed steel are shown in figure 2.2 [14].

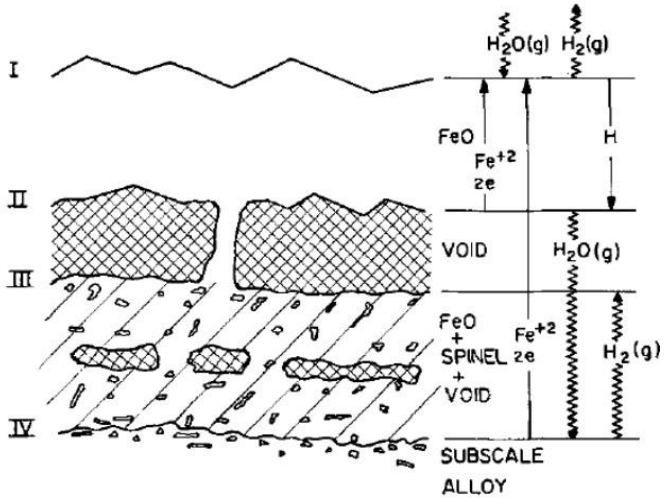

Figure 2.2: The mechanism for oxidation of Fe-Cr alloys in the 'wet' condition [14]

The water vapour is firstly adsorbed on the clean metal surface and it reacts with metal ions to produce wüstite (FeO) and hydrogen (H_2) [14]. These reactions are shown below [14]:

$$\boldsymbol{H_2O_{(g)} \rightarrow H_2O_{(ads)}} \qquad \textbf{Eq. 2.1}$$

$$\boldsymbol{H_2O_{(ads)} + Fe^{2+} + 2e^{-} \rightarrow FeO + Fe_{vac} + 2 \oplus + H_{2(ads)}} \qquad \textbf{Eq. 2.2}$$

$$\boldsymbol{H_{2(ads)} \rightarrow H_{2(g)}} \qquad \textbf{Eq. 2.3}$$

$$\boldsymbol{H_{2(g)} \rightarrow 2H^{*}} \qquad \textbf{Eq. 2.4}$$

Where the Fe_{vac} presents the vacant iron ion site, presents an electron defect and *H* means the hydrogen atom in the oxide film.

At interface II in figure 2.2, iron oxide is dissociated to produce an oxide ion. These oxide ions can be treated as the absorbed species, which can react with infusing hydrogen to form a carrier gas. The carrier gas provides oxygen transport to the forming pore [14]. The reactions are shown below;

$$\boldsymbol{FeO + Fe_{vac} + 2 \oplus \rightarrow Fe^{2+} + O^{2-}} \qquad \textbf{Eq. 2.5}$$

$$\boldsymbol{2H^{*} \rightarrow H_{2(ads)}} \qquad \textbf{Eq. 2.6}$$

$$H_{2(ads)} \rightarrow H_{2(g)} \qquad \textbf{Eq. 2.7}$$

$$H_{2(ads)} + O^{2-}_{(ads)} \rightarrow H_{2(g)} + 2e^{-} \qquad \textbf{Eq. 2.8}$$

Finally a wustite layer forms as the outer layer, at the interface between the oxide and air/water [14].

Low carbon steel and T22 (power plant grade steel containing approximately 2.5 wt% Cr and 0.5-1 wt% Mo), have relatively poor oxidation resistance in steam (wet condition), which means they are used in components that experience lower temperatures that more commonly used in power plant[15]. These steels (Low carbon steel and T22) form oxide scales consisting of magnetite and haematite at temperature below 560 ℃. With increasing temperature, wustite (FeO) also forms and a spinel oxide will form if the steel is alloyed [15].

P91, an alloyed martensitic power plant steel, which has a higher Cr content (typically 9 wt- %), has a higher oxidation resistance in a steam environment. It can be used at high pressures (300bar) and high temperatures (620 ℃) [15].

2.1.2. Reaction kinetics

By measuring the amount of oxygen or metal consumption or the amount of the oxide produced (by weight or thickness), the oxidation rate can be measured experimentally. In these methods, metal consumption is the least preferable for its destructive, indirect and discontinuous nature. All these methods can be measured as a function of time to show the rate of oxidation [11]. Three main rate laws have been observed from experimental data, when there is no spallation or break up of the oxide, and are described below;

- The linear law: the rate of oxidation is constant with time. This relationship can be observed at the initial stages of the oxidation, which can be described by the following equation [8],

$$x = k_1 t \qquad \textbf{Eq. 2.9}$$

  where x is the oxide thickness, k_1 is the linear rate constant and t is the time [8].

- The parabolic law: the rate of oxidation is inversely proportional to the square root of time. This relationship tends to be observed for oxidation at high temperature, and is described by the following equation,

$$\mathbf{x^2 = 2k_2 t} \qquad \textbf{Eq. 2.10}$$

  Where $\mathbf{k_2}$ is the parabolic rate constant [11].

- The logarithmic law: this tends to happen at low temperatures (usually below 300-400^{0}C) and results in an oxide film that is less than tens of nm thick [10].

  The first two laws are shown graphically in figure 2.3

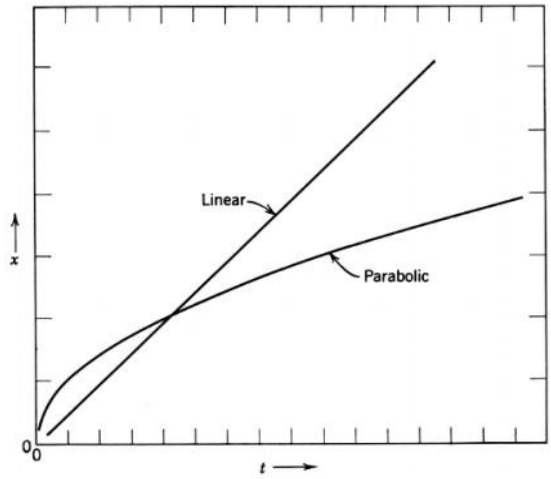

Figure 2.3: *Graph showing the linear and parabolic relationships of oxidation where oxide grows as the function of time [8]*

Fernandez had researched the isothermal oxidation curves of the different steels at 500 and 600^{0}C shown in figure 2.4[16]. With the increasing of content of Cr the weight gained decreased due to the high oxidation resistance.

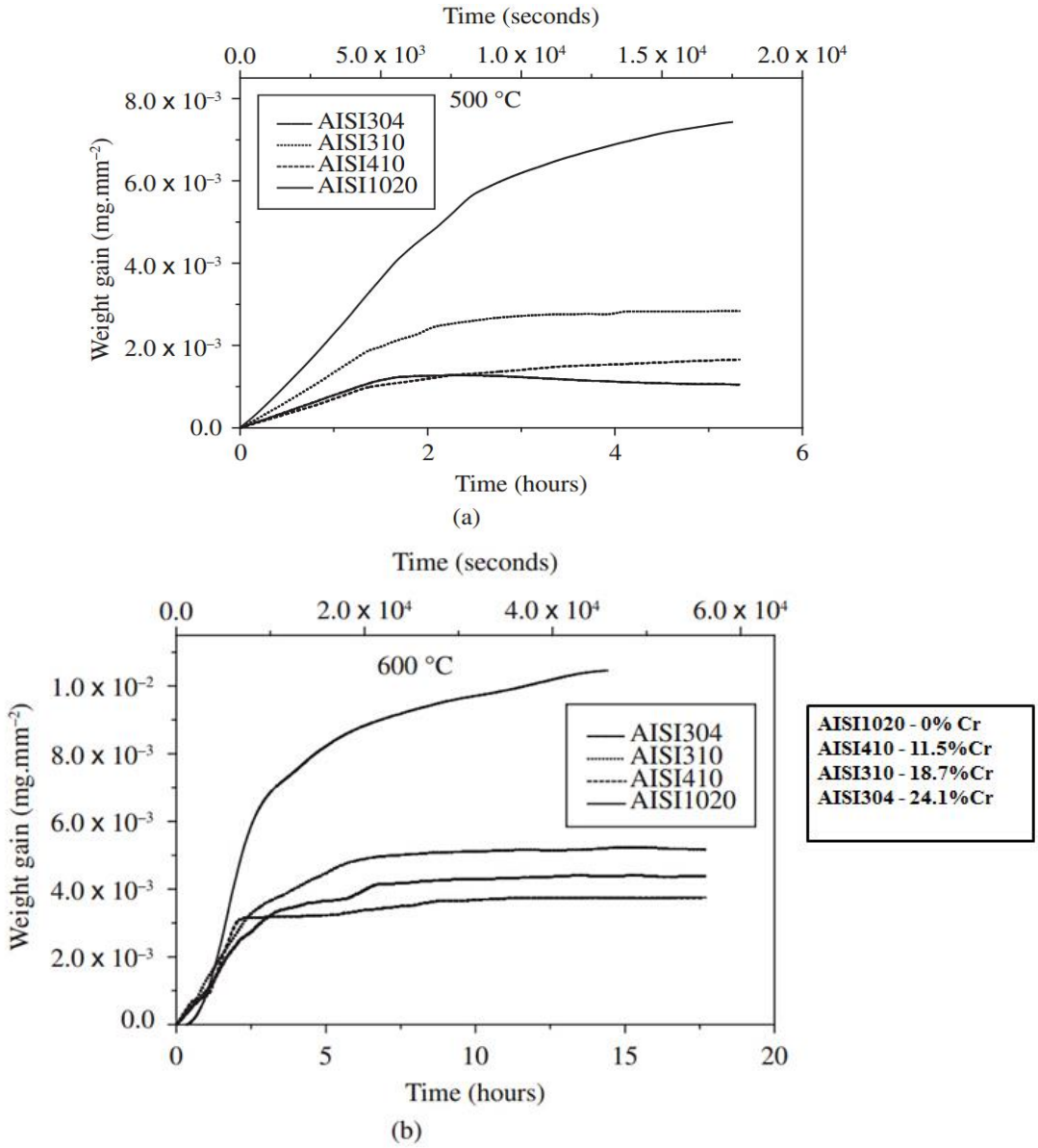

Figure 2.4: Oxidation behaviour of steel at (a): 500 and (b): 600 ^{0}C [16]

The measured oxidation kinetics for pure iron in oxygen and in steam at 650-750^{0}C, reported by Juntao Yuan, is shown in figure 2.5(a) [40]. It can be seen that the weight gain in dry oxygen is always smaller than that in wet oxygen, and the weight gain at high temperature is larger than that at low temperature. Figure 2.5(b) shows that oxidation follows a parabolic plot in dry oxygen and in steam. The reaction kinetics in steam at all temperatures shows the trend to be initially linear and then parabolic [40].

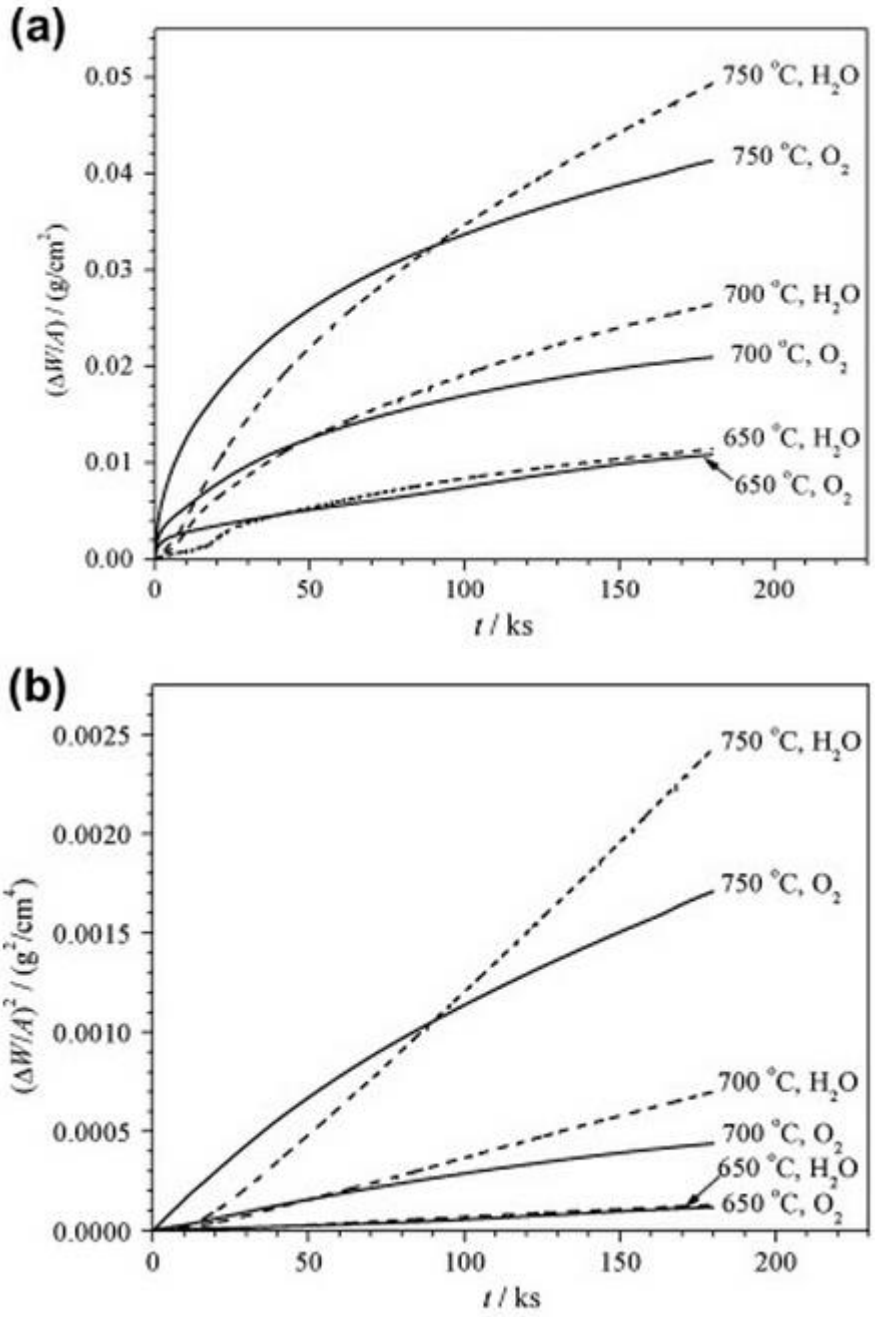

Figure 2.5: (a): Oxidation kinetics in dry air and in wet air; (b): Parabolic plot of oxidation kinetics in dry air and in wet air[40].

2.1.3. Oxide spallation

The new-formed oxide usually forms with an associated mechanical stress due to the lattice mismatch between the oxide and metal substrate. When the stress in the oxide is high enough (usually when the oxide becomes thicker), the oxide scale will deform or even break. The internal compressive stress in the oxide (for an oxide that occupies a larger volume than the volume of the metal it formed from) is balanced by a tensile stress in the metal, in the absence of any external stress. When the stresses cannot be tolerated at the interface between the oxide and metal the oxide film tends to spall off. Stresses can be developed by oxidation or by temperature change, due to the different thermal expansivities of the metal and oxide [11,12].

With continuous diffusion of oxygen and/or metal ions, the volume of oxide film will change; however, unequal mixed transport (oxygen and metal ions) can become possible as a result of micro-cracks and porosity. To ensure the same growth rate of the inner and outer oxide layers, to then minimize the stresses that form, controlling alloy chemistry of both metal and oxygen ions is required.

Figure 2.6 shows the effects of metal surface curvature on the growth stress development in oxide scales [12]. For low carbon steels the oxidation reaction typically progresses initially by oxygen diffusion to the metal-oxide interface to give a larger volume than the metal it replaces, therefore, from figure 2.6, it can be seen that oxidation on a convex surface (such as the outside of a boiler tube) would result in a build-up of tensile stresses in the oxide. For steel tubes where there is dry oxidation on the outer surface of the tube, which makes the dominant growth mode driven by oxygen diffusion to the metal interface, then tensile stresses develop in the outer oxide layer which is more likely to give cracking.

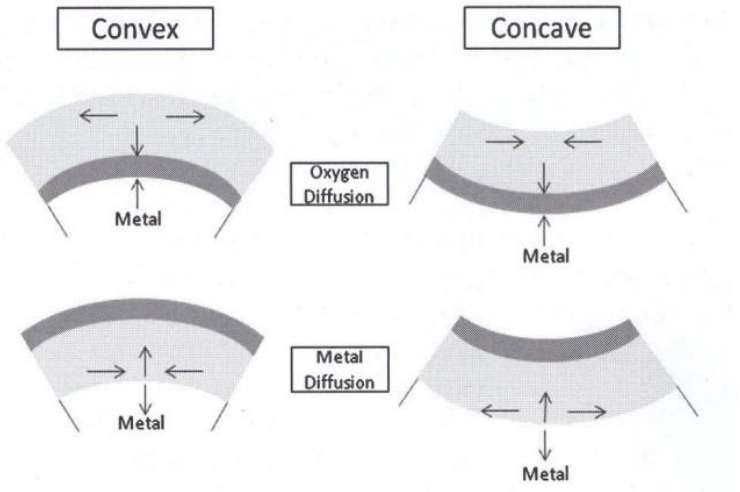

Figure 2.6: The effects of specimen geometry on scale growth stresses with the dark grey shading signifying newly grown oxide [12].

2.1.4. Oxidation resistance

P91 has relatively high chromium content (approx 9 wt%), forming a protective and slow growing chromia oxide layer [17], which helps improve the hot corrosion resistance of pipes used in steam work. The inward diffusion rate of oxygen in the oxide is much slower than the outward diffusion rate of Cr along grain boundaries in the metal, which indicates that as the oxide film forms, the oxidation rate will slow down. Chromium content is a vital factor deciding the nature of the oxides formed e.g. steels with a low chromium content (< 2 wt%) form a mixed Fe/Cr oxide which, whilst more protective than FeO, is less protective than a full chromia layer [18]; steels with a greater chromium content (>13 wt%) show lower oxidation rates due to the inner layer consisting of pure Cr_2O_3, $(Cr, Fe)_2O_3$ or $(Cr, Fe_xMn)_3O_4$ and an outer layer of Fe_2O_3 and Fe_3O_4 [19].

Silicon and manganese additions are also well known for improving the oxidation resistance of steel alloys [20]. Adding Si has been reported to increase the adhesion of the chromia layer, or the inner layer being enhanced by the formation of a continuous silica layer to preventing ions diffusing and hence reducing the oxidation rate. [18]. Manganese has been suggested to form a protective $MnO.Cr_2O_3$ layer which reduces oxidation rates [21].

2.1.5. Oxide films on iron and alloys

Multiple-oxide phases can form on iron after long term oxidation, an example of which is shown in figure 2.7. The nature of the oxide changes (from the surface towards the metal) from oxygen-rich to metal-rich; i.e. from Fe^{3+} in hematite to a mixture of Fe^{2+} and Fe^{3+} in intermediate magnetite; and then a final inner layer of predominantly Fe^{2+} in FeO (wustite). The formation of an intermediate magnetite layer has been reported to only take place at 350-570^{0}C, by the reduction of hematite with iron or oxidation with air and water [22]. It can be seen that for pure iron heat treated in dry air at 600 ℃ the wustite layer dominates in terms of thickness, figure 2.7. It can also be seen that pores exist in the oxide films, for example in figure 2.7 significant porosity is evident at the wustite – metal interface, also within the wustite as well as within the magnetite and hematite layers.

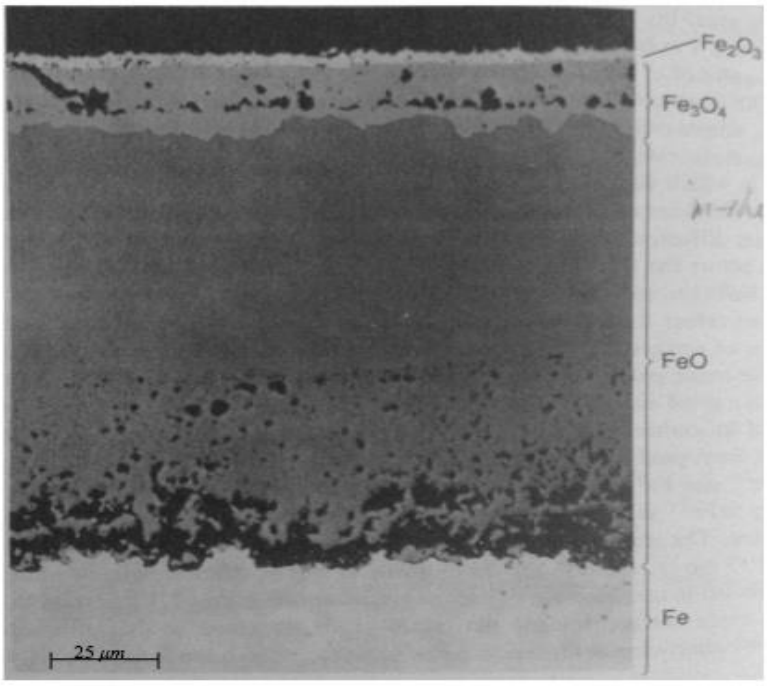

Figure 2.7: Microstructure of iron oxides formed on iron by long term high-temperature (600 ℃) oxidation in air [22]

P91, 9-12% Cr, martensitic steels, are widely used in steam turbines, which can be exposed to a high pressure and high temperature environment. The main alloying element added in the P91 steel is Cr, to provide oxidation resistance due to the protective Cr-rich oxide layer that forms. During oxidation in a steam atmosphere it

was reported that the outer layer that formed is Fe-rich and forms by outward diffusion of Fe ions reacting with OH^- ions from steam, to give a magnetite layer. An initial inner oxide is formed by Fe and Cr ions [23]. Dogan also has reported that P91 steel will form $Mn_{1.5}Cr_{1.5}O_4$ and $FeMnO_3$ in dry air at 650 ^{0}C, meanwhile it will form $FeCr_2O_4$ in moist air at 650 ^{0}C [9] The growth of oxide on P91 (after 1, 2, 7 and 16 hours) after oxidation in N_2-1vol%O_2-2vol%H_2O at 650 ^{0}C is shown in figure 2.8 [3].

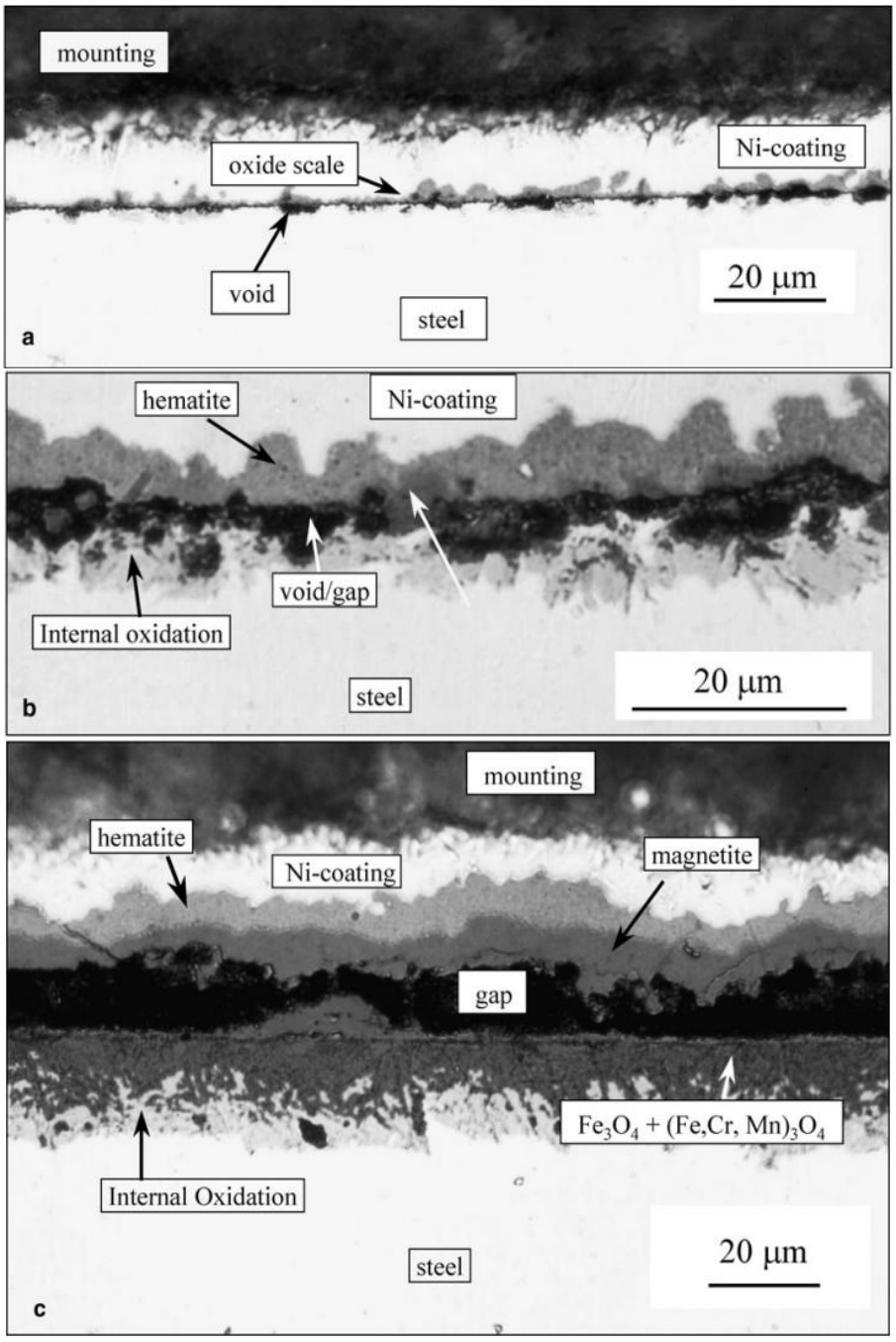

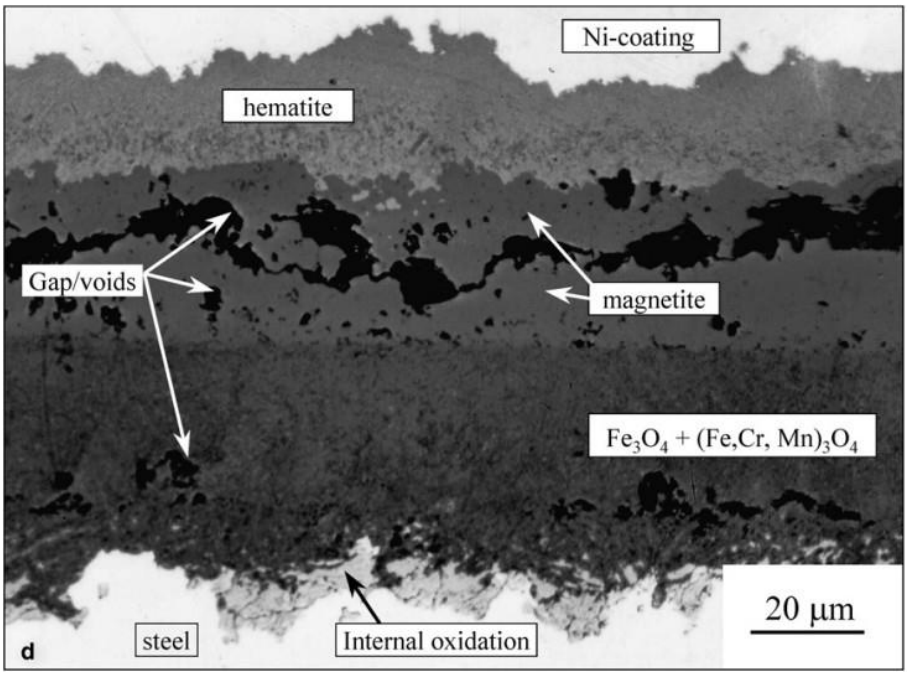

Figure 2.8: Metallographic tapered cross-sections of oxide scales on P91 after oxidation in N_2-1vol%O_2-2vol%H_2O at 650 ^{0}C: (a) 1 hour, (b) 2 hours, (c) 7 hours, (d) 16 hours. Specimens were mirror-polished prior to oxidation [3]

It can be seen that the oxide thickness shows different values (total oxide thickness of approximately 1, 8, 50 and 100 µm) with different oxidation times (1, 2, 7 and 16 hours). There was evidence (shown in figure 2.9) in the XRD results of the presence of iron oxide after oxidation for 30 hours.

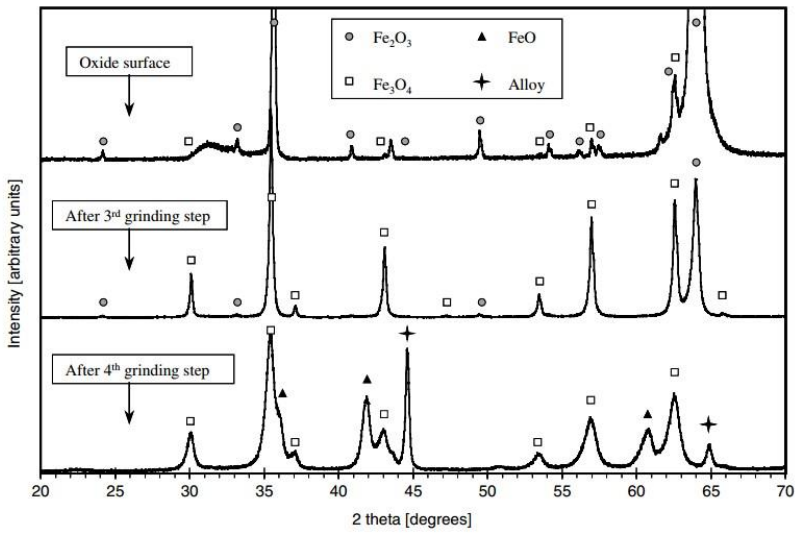

Figure 2.9: XRD patterns of the oxide scale formed on P91 during oxidation for 30 h in N_2-1vol%O_2-2vol%H_2O at 650 ^{0}C [3]

Figure 2.10 shows that the presence of water vapour may also increase the oxidation rate as it was reported that it can provide conditions for breakaway oxidation of P91 steel [3, 24].

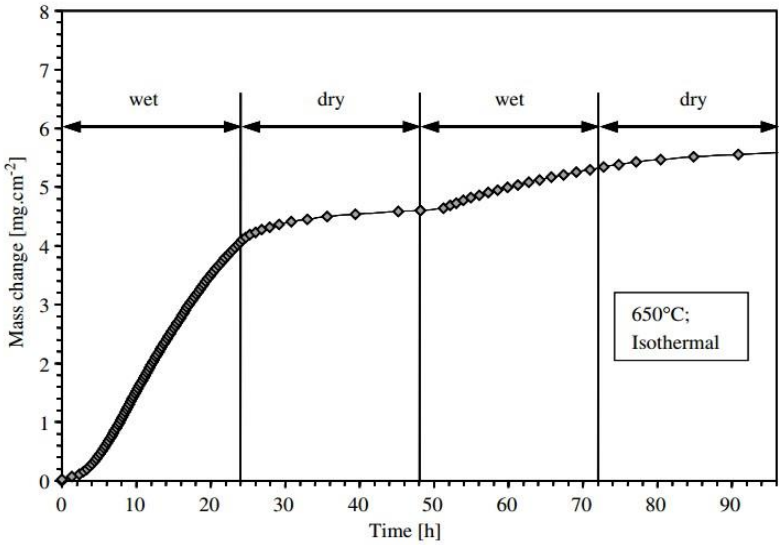

Figure 2.10: Oxidation kinetics of P91 in oxygen and steam every 24hours at 650^0C[3]

T22 grade (2-2.5 wt% %Cr) is a low alloy ferritic steel that is used in pressurized applications and also in heat recovery steam generators [22]. On examining T22 boiler tubes after service (exposed at temperatures of approximately 600 ℃), it was found that the composition of the scales formed was predominantly magnetite and wüstite. Researchers have examined the microstructure of oxide scales grown on T22 ferritic steel at 550 ℃ for 300 hours in the condition of flowing steam (shown in figure 2.11 (a)) [25]. The oxide thickness of T22 in this treatment is about 85 μm. Compared to the P91 steel (9-12%Cr), where 30 μm oxide layer formed with the same treatment (shown in figure 2.11(b)) [25], the T22 steel (lower Cr content) shows a lower oxidation resistance than P91 [23, 26, 27].

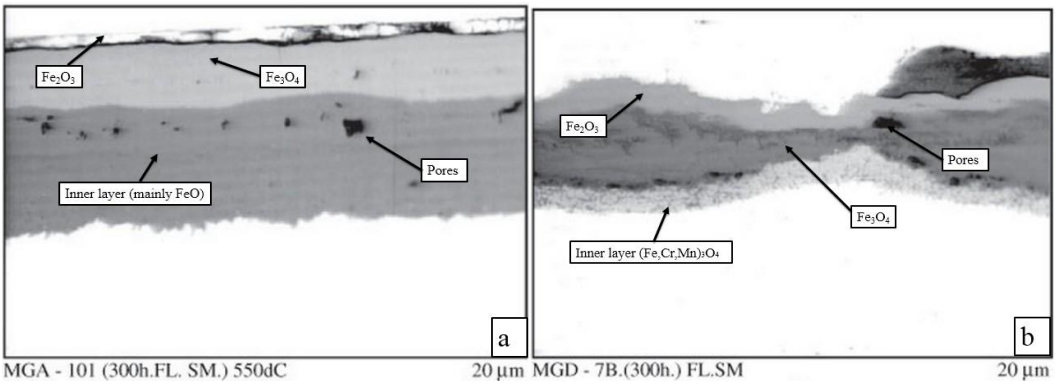

Figure 2.11: Microstructure of oxide layer on (a):T22 steel (b):P91steel at 550 ℃ for 300h in flowing steam [25]

2.2. EM fundamentals

2.2.1. Relative permeability

A magnetic field can be represented by magnetic lines of flux and the total number of lines through a unit area is termed as the magnetic flux density (B), which is related to the materials magnetic permeability and the field strength (H), this is shown by equation 2.11 [28]. When applying a current to a multi-turn coil (exciting coil shown in figure 2.12), a magnetic field will be produced and the field strength H can be determined from equation 2.12 [28] below:

$$B = \mu_0 \mu_r H \qquad \textbf{Eq. 2.11}$$

$$H = \frac{NI}{L} \qquad \textbf{Eq. 2.12}$$

Combining equations 2.11 and 2.12 gives

$$B = \frac{\mu_0 \mu_r NI}{L} \qquad \textbf{Eq. 2.13}$$

Where B is the magnetic induction (T), μ_0 is the magnetic permeability of free space in Henry. m^{-1}, N is the number of turns in the coils, I is the current (A) and L is the length of the coil (m), μ_r is the relative permeability of the sample. *(The direction of the field has to be within the coil.)*

There are two main types of EM sensors used in the previous research on microstructural characterization; air-cored and ferrite-cored sensors [6]. These have different sensitivities to materials with different magnetic permeability values. In previous work it was shown that ferrite cored sensors were more sensitive to microstructure changes when testing materials with higher permeability [6].

A typical EM sensor consists of one exciting coil and four sensing coils. The exciting coil is driven by an impedance analyzer which gives an AC current, thus a variable magnetic field is generated [7]. A typical H-shaped EM sensor used in recent research is shown below [29]:

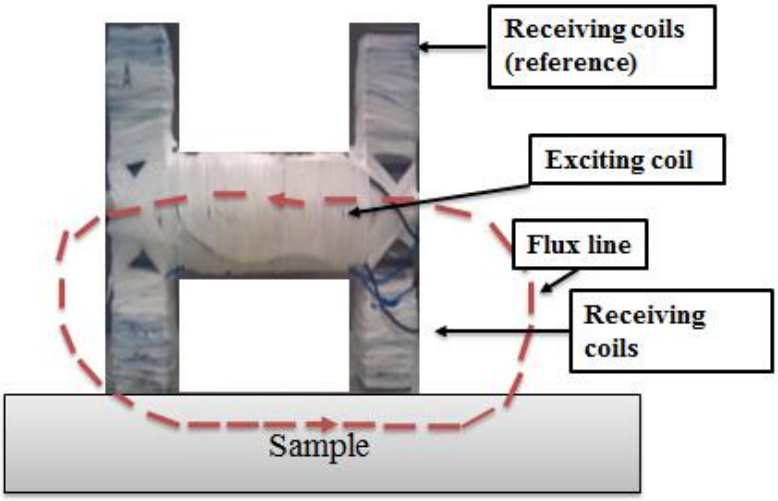

Figure 2.12: Schematic diagram of a H-shaped EM sensor [29]

The flux lines generated by the exciting coil will interact with the sample, and pass through the receiving coils, as shown in figure 2.12[33]. Note that there are two pairs of sensing coils in the H-sensor shown in figure 2.12, one pair can be used for a background reference signal, whilst the pair near the sample are used for materials measurements. Any changes in the magnetic field caused by the sample will induce a voltage in the measurement sensing coil. This process is called the mutual inductance (M_L), and is given in equation 2.14 [28].

$$\boldsymbol{M_L = \frac{N_1 N_2 \mu_0 \pi_r}{l}} \qquad \textbf{Eq. 2.14}$$

Where M_L is the mutual inductance in Wb/Amp, N_2 is the number of turns in the sensing coil; μ_0 is the magnetic permeability of free space in henry/m, μ_r is the relative permeability of the sample and A is the cross section area of the coils. **I** is the electric current through the exciting coil in Amp.

The sample's relative permeability is not the only parameter that influences the inductance reading. The electrical currents in the specimen may cause a change in the real inductance when a time-varying external magnetic field is applied [30]. Any change in the permeability and/or electrical resistivity of the target material contributes to a change in the induced field. Eddy currents in the sample at low test frequency are low and the electromagnetic field can go through into the sample [31].

Therefore, the mutual inductance (M_L) is mainly influenced by the relative permeability of the sample during low frequency testing.

With an increase in the test frequency, eddy currents, which oppose the driving current, become more dominant and the coil mutual inductance decreases [31]. Therefore, the mutual inductance is influenced by the magnetic permeability and electrical resistivity of the sample at higher frequencies.

The depth the electromagnetic field can go through into the sample is called the "skin depth" and is given in equation 2.15, [32] It can be seen that the skin depth will decrease with increasing frequency and is dependent on the material parameters of resistivity and relative permeability.

$$\mathbf{d} = \sqrt{\frac{2\rho}{2\pi f \mu}} \qquad \textbf{Eq. 2.15}$$

Where d is the skin depth in m, ρ is the resistivity of the material in $\Omega \cdot$ m, f is the frequency of the AC current in Hz and μ is the relative permeability (no unit).

2.2.2. Previous work using EM sensors to determine microstructure in steels

Previously, EM sensors have been shown to be able to monitor the austenite-ferrite phase transformation in steel [6]. X.J. Hao also found that decarburisation layers at the surface influence the EM signal for pearlitic steels [5]. He found that the multi-frequency EM sensor showed potential for measuring the decarburization content of steel bar industrially [5]. Figure 2.13 (a)-(d) shows the microstructures of Fe-0.8wt.%C steel after decarburizing at 1000^0C for 10mins, 1h, 2h and 5h, while figure 2.13(e) shows the measured inductance changes with frequency for the decarburized samples [5]. It can be seen from figure 2.13 (e) that the inductance values (EM sensor signal) increase with an increase in heat treatment time, and hence decarburized layer. This was reported to be due to the decarburized layer (predominantly ferrite) having a higher relative permeability than the bulk pearlite microstructure.

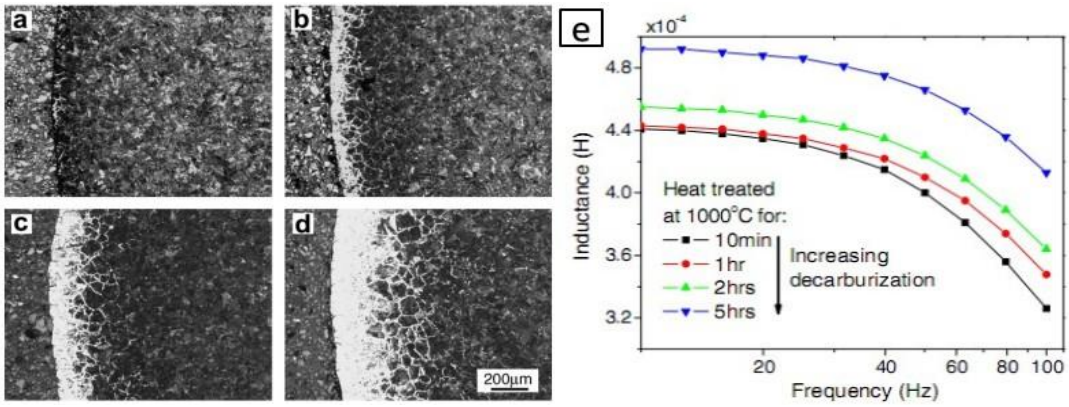

Figure 2.13: Microstructures of decarburised samples (a) 10min, (b) 1h, (c) 2h, and (d) 5h. (e) Measured inductance changes with frequency for decarburized samples.

L. Zhou's recent research had shown that steels with different carbon contents, giving different ferrite-pearlite phase balances, could be detected by multi-frequency EM sensor testing [7], as shown in Figure 2.14. He also had found that the real inductance increases with the increased grain size, shown in figure 2.15.[7] In addition, it has been shown that the EM sensor can also monitor steel with different amounts of plastic or elastic strain [33].

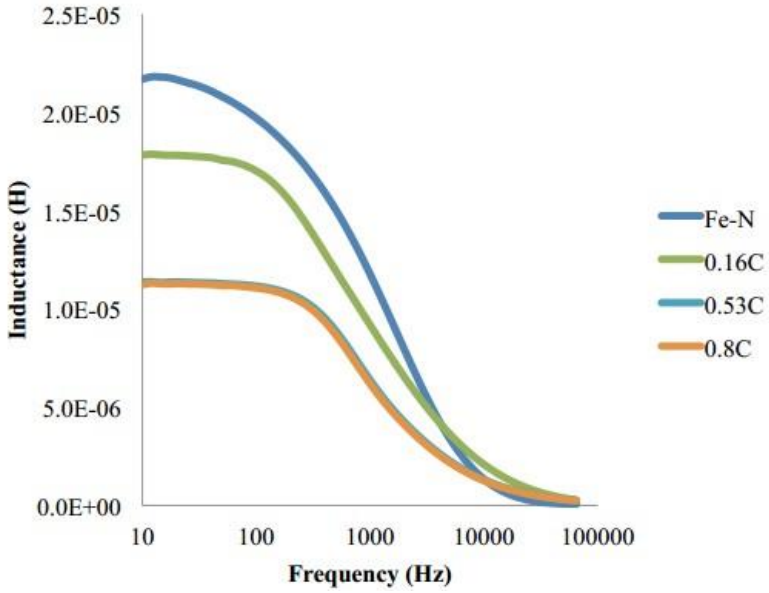

Figure 2.14: Real inductance changes with frequency for Fe-N (nominally pure iron), 0.16C, 0.53C and 0.8C steel samples. (The pearlite fraction was measured to be 0%, 4.3%, 90% and 100% respectively)[7]

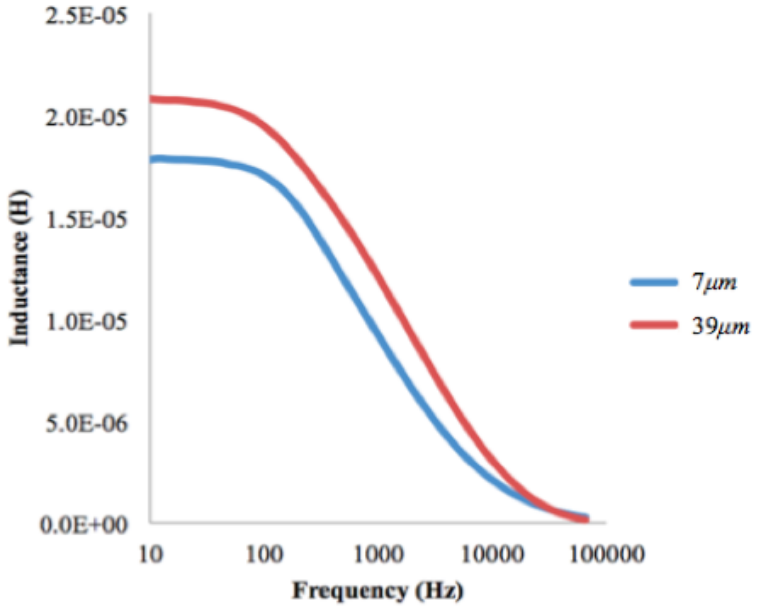

Figure 2.15: Real inductance changes with frequency for 0.17C steel heat treated to give grain sizes of 7μm and 39μm [7].

When Hao et al. used multi-frequency EM sensors to measure the ferrite fraction from 0% to 100% in austenite-ferrite dual phase steel microstructures, shown in figure 2.16, it was found that the real inductance, which is related to the relative permeability of the samples, increased with ferrite percentage [6]. The relative permeability of austenitic steel equals 1 (i.e. paramagnetic), which is similar to the values for hematite and wüstite shown in Table 2.1. However, magnetite has a relative permeability of approximately 200-240, which is similar to that of ferritic steel [6], although it has a much lower conductivity.

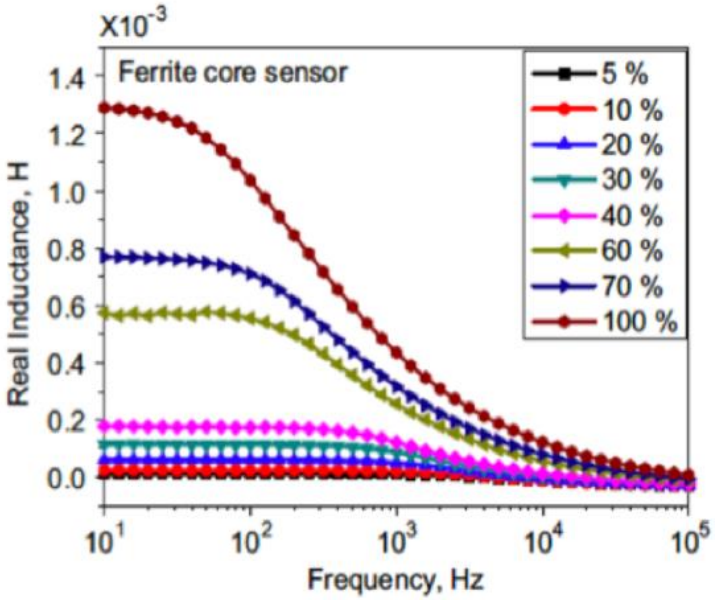

Figure 2.16: Real inductance versus frequency at ferrite fraction of 5%-100% [5]

Liu et al have researched the relationship between the EM signal and microstructure in T22 and P9 steels after heat treatments and in-service exposure (at elevated temperatures) as shown in figure 2.17. They found that heat treatment causes the fine tempered martensite laths to coarsen, eventually giving equiaxed ferritic grains, and the fine M_2X carbides to change to larger $M_{23}C_6/M_6C$ carbides, which increases the real inductance value at low frequencies, as measured by the EM sensor [34].

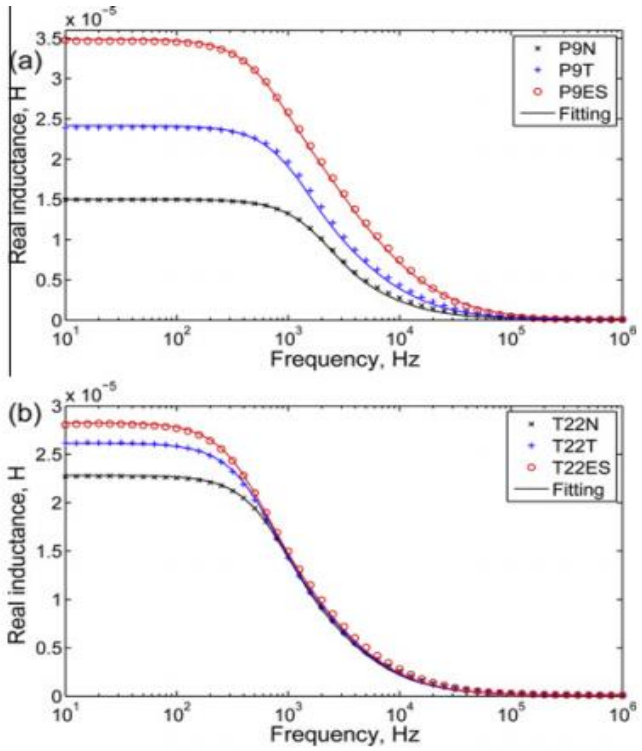

Figure 2.17: Real mutual inductance of EM sensor coils as a function of frequency for (a) P9 and (b) T22. (N-normalized; T-tempered; ES-service-exposed) [34]

2.3. Commercial NDT systems for use in power-plant applications

Several NDT techniques are currently used in inspecting the power-plant system (boiler tube and heat exchangers; where the materials used are ferromagnetic and non-ferromagnetic steels mentioned before). There are three main electromagnetic systems used in inspection of power-plant steels.

2.3.1. Eddy Current (ET) Method

The eddy-current inspection technique monitors the changing inductance of a coil. The electrical currents in the specimen cause a change in the real inductance when a time-varying external magnetic field is applied [30], figure 2.18, which is similar to the EM sensor approach described earlier. Any change in the permeability and/or electrical resistivity of the material contributes to the different induced field. ET method is widely used to detect cracks on the surface of a component due to the skin depth effect. It has been reported that the ET method can measure local changes in

residual stress when using automated scanning equipment [30].

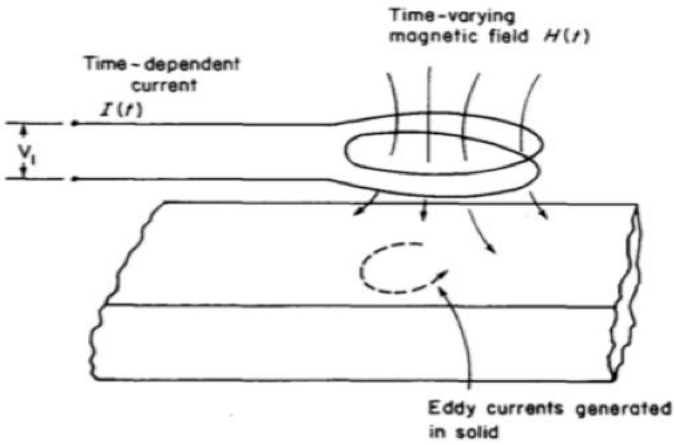

Figure 2.18: Schematic diagram showing the eddy-current testing approach [30].

2.3.2. Remote field eddy current examination method

Remote Field Eddy Current (RFT) is based on the transmission of an external electromagnetic field though the tube. There are some similarities with the ET method, but the exciting coil shown in figure 2.19 generates eddy currents at a low frequency to ensure that the electromagnetic field is transmitted through the tube thickness and travels on the outer surface. The receiver coil will receive the remote field signal and the output can be monitored on screen. For an application of inspecting water pipes then the equipment set up involved the receiving coil being set at four times the tube diameter from the exciting coil (shown in figure 2.19). Flaws, dents and defects will cause a disturbance in the through-transmission path, which will influence the remote field eddy current shown by the voltage plane curves monitored on the screen, it also has a relative high resolution[35]. The RFT technique is now a well-established method for detecting defects in ferromagnetic tubes since conventional eddy current techniques have difficulty inspecting the total thickness of the tube wall, and it also applicable to paramagnetic (austenitic stainless steel) tubes.

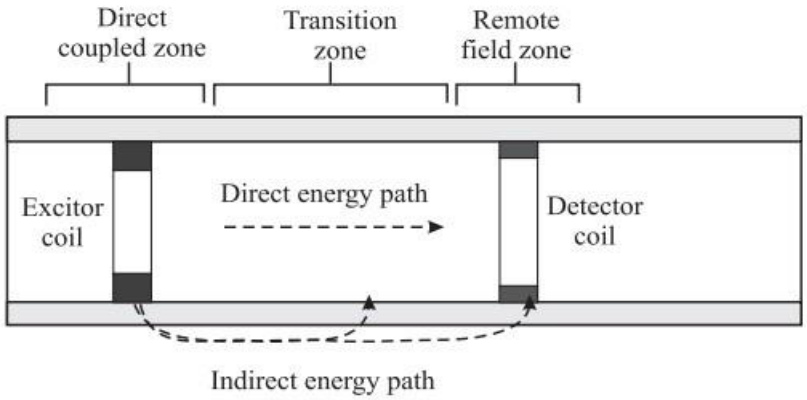

Figure 2.19: The principle of remote field eddy current testing [35].

2.3.3. Ferroscope TT. (Though transmission) instrument

In stainless steel (super-critical) boiler tubes, the exfoliation of magnetite flakes tends to happen when going through the heat cycles. And the magnetite flakes keeps falling down in the tubes, which tend to accumulate the tube bend sections and eventually cause magnetite blockage in the bends. This will choke off the steam flow, when the blockage exceeds a certain limit leading to tube failure [38]. Ferroscope TT had shown its advantages in detecting the magnetite blockages in stainless steel tubes using through transmission electromagnetic technique. As the permeability of magnetite is far more than that of stainless steel, it makes possible for Ferroscope TT instruments to detection magnetite in non-ferromagnetic stainless steels [38]. This technique had indicated the importance of oxidation on NDT signals.

2.4. Summary

From the literature review it can be seen that EM monitoring systems can be used to detect changes in the microstructure of steels due to changes in the magnetic relative permeability and electrical conductivity. It is known that steels form complex oxide films during high temperature exposure (in dry and wet conditions), but so far there have been no reports on the effect of different oxide film types on EM sensor signals. In addition there is no data available on the effect of oxide film thickness on the EM signals in plain carbon steel, T22 and P91 power plant steels.

3. Experimental procedure

3.1.Materials and microscopy

Three steels, two grades that are widely used in power plant (T22 and P91 grades) and plain carbon steel (CS), have been studied. The chemical compositions of the steel samples are given in Table 3.1. The material conditions are shown in Table 3.2.

Table 3.1: Composition (wt %) of the plain carbon steel (CS), T22 and P91 steels [7, 34]

	C	**Mn**	**S**	**Si**	**Cr**	**Mo**	**P**	**Cu**
CS	0.17	0.67	0.036	0.17	-	0.016	0.024	0.3
T22	0.11	0.5	0.011	0.5	2.30	0.09	0.02	-
P91	0.10	0.4	0.010	0.30	9.0	1.00	0.02	-

Table 3.2: As-received material conditions

Samples	**Conditions**
CS	5.1 mm thick plate that had been reaustenitised and oil quenched
T22	3.9 mm thick plate (hot rolled, normalised and tempered) taken from service after approximately 11 years at 520 ℃
P91	10.2 mm thick plate. Normalized at 1050 ℃, air cooling down to 200 ℃, then tempered at 760 ℃ for 5 hours

3.2. Characterisation

Samples, before and after the oxidation heat treatment, were sectioned and mounted in conductive bakelite, then manually polished to a 9 µm finish using a Mol cloth and a 6 µm finish using diamond suspension, followed by polishing using in a Nap cloth and 1 µm diamond suspension, and etched in 2% Nital (plain carbon steel and T22) or Kallings reagent (P91). The optical microstructure was characterized using a Zeiss optical microscope.

The hardness of the steels was measured on polished samples by Vickers micro hardness measurement with a 500g load. Each hardness value was determined by taking the average of 4 measurements.

To measure the oxide film thickness five measurements (perpendicular to the oxide surface) were made using ImageJ software – measurements were made equi-distantly on each micrograph (a total of four micrographs for each heat treatment condition were measured), an example is shown in figure 3.1. The mean value and standard deviation value for the oxide thickness were calculated from the 20 measurements made. As the oxides form initially with a nodular and discontinuous structure these measurements have relatively high standard deviation values, especially for the short term (25 hours) heat treatments.

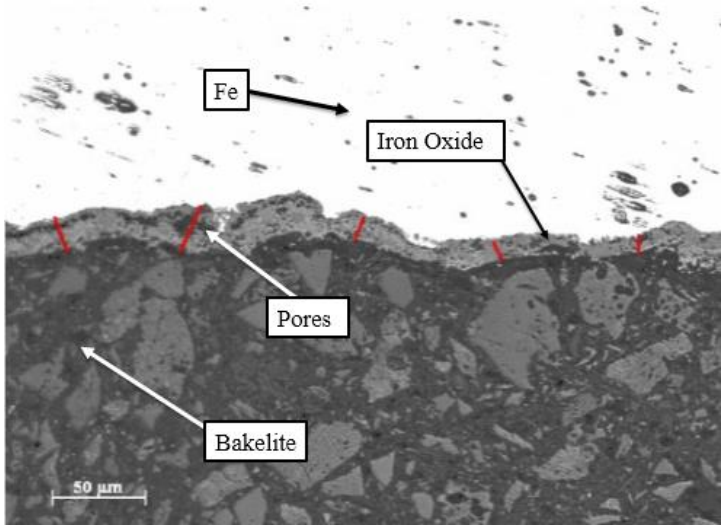

Figure 3.1: Optical metallography image showing how the oxide thickness measurements were made

To measure the porosity in the oxide films, measurements were made using ImageJ software on three different micrographs. The percentage of pores in each sample was calculated as the proportion of red region over the total oxide proportion, which is shown in figure 3.2.

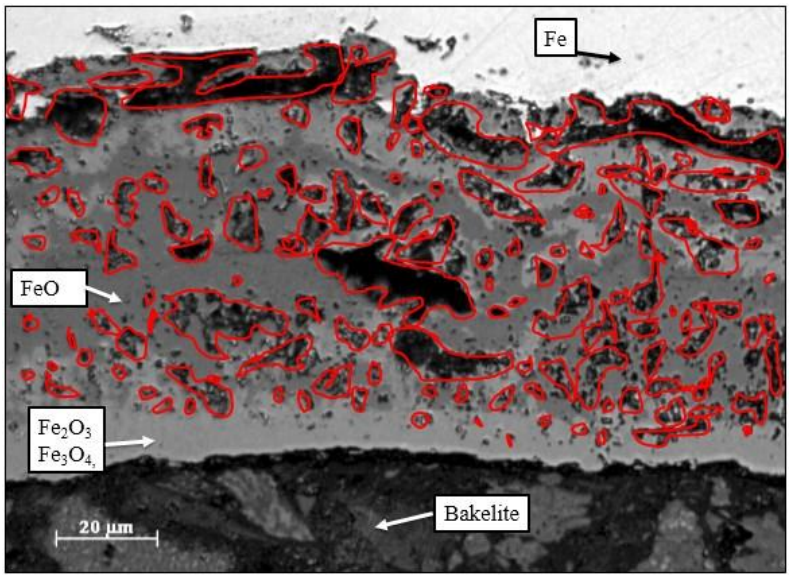

Figure 3.2: Optical metallographic image showing how the pore percentage was determined.

3.3. EM sensor

A schematic diagram of the EM sensor used in this work is shown in figure 3.3. An impedance analyzer (S1260) (shown in figure 3.4) was used to drive the exciting coil at frequencies from 10Hz to 65000Hz, and then the real inductance values were measured from one side of the sensing coils.

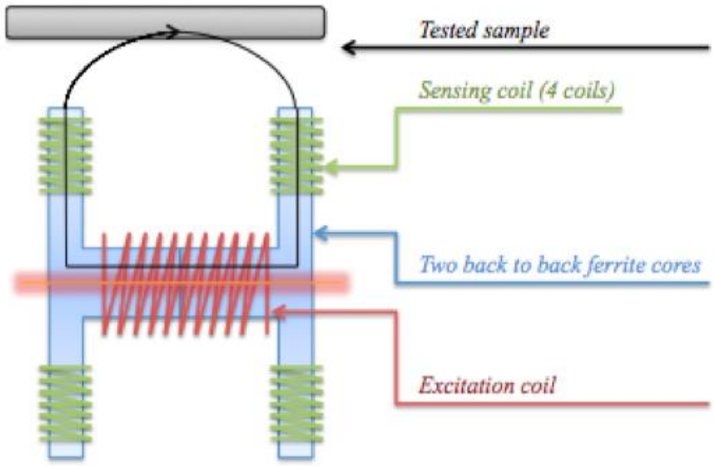

Figure 3.3: Schematic diagram of the H-shaped EM sensor used in this work.

Figure 3.4: Photograph of the impedance analyser (S1260).

3.3.1. Edge effect

It is known that electromagnetic signals are affected by the geometry of the test specimen, with an edge effect (when measuring close to a sharp corner / edge of a sample) having a large effect [33]. In order to test the edge effect, the EM sensor was set parallel and perpendicular to the sample edge with different distances (from 0mm to 10mm by 1mm step) from the edge using a rectangular rail steel sample (103mm length, 45mm width and 10mm thickness) at a frequency of 1000Hz, shown in figure 3.5(a). The edge effect results in the real inductance value, for the case of the multi-frequency EM sensor, gradually decreasing with increasing distance when the sensor is perpendicular to the edge, as shown in figure 3.5(b). When the sensor is parallel to the edge of the sample, it is found that the decreasing distance to the edge does not affect the real inductance signal until the EM sensor is over the edge of the sample, figure 3.5(b). Therefore, measurements were made with the EM sensor at least 10mm from the edge of the heat treated samples so that there was no edge effect on the measured inductance values.

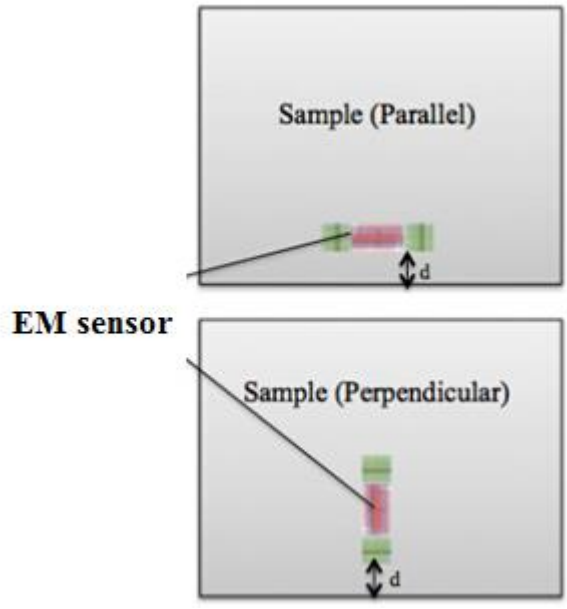

(a).

(b).

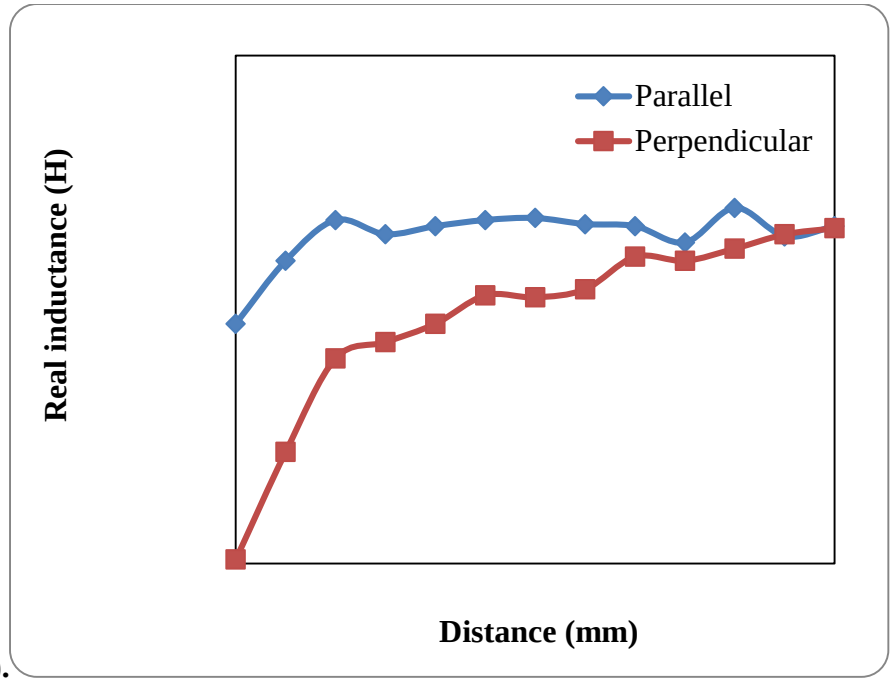

Figure 3.5: (a): Edge effect test (b):The real inductance with distance from the edge of a sample (0.8wt% C plain carbon steel plate) for parallel and perpendicular orientations of the EM sensor

3.4. Lift-off tests

To determine the relationship between the EM sensor signal and lift-off, measurements of the inductance value at 100Hz were made. The real inductance values for the plain carbon steel samples using the EM sensor are discussed in section 4.4 for nominal lift-off, d_x, values of 0 – 1.04 mm. The (inherent lift-off in the EM sensor) d_0 is 0.35mm due to the position of the sensing coils from the base of the sensor. Nominal lift-off values of 0 mm, 0.26 mm, 0.52 mm, 0.78 mm and 1.04 mm were tested by using pieces of plastic of known thickness to act as a spacer between the steel sample and EM sensor, shown in figure 3.6.

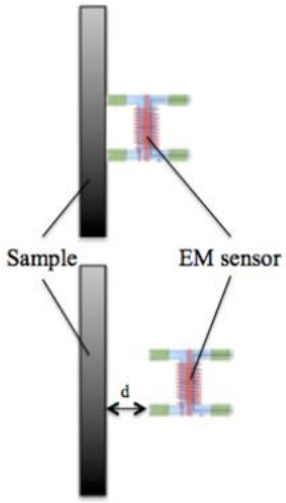

Figure 3.6: Lift-off effect test

3.5. Heat treatments and EM testing

Samples, before and after heat treatment, were tested using the H-shaped EM sensor. The surface of the samples before initial EM testing and before heat treatment was prepared to a 120, 240, 400, 800 and then 1200 grit sandpaper and polishing finish. All the samples were cleaned between stages with tap water and degreaser, with a further clean in ethanol and hot air dried before the polishing stage.

Heat treatments in an air furnace at 700^0C (25 and 75 hours) and 650^0C (25, 50 and 75 hours) were carried out on samples measuring approximately 142.4(length) x 28.4 (width) x 3.9 (thickness) mm (T22), 42.6 x 23.4 x 10.2mm (P91) and 28.4mm (radius) 5.1mm (thickness) (CS) of as received material. EM testing was carried out before heat treatment with the sensor in contact with the samples; three measurements were taken on each sample and the average value and standard deviation calculated. The oxidized samples were then EM sensor tested without any further surface preparation.

Samples were tested with the EM sensor at a fixed frequency (100 Hz) to investigate the effect of the thermal exposure on the steel microstructure by removing the oxide films using grinding. The surface finish was prepared to a grit sandpaper finish, for consistency with the pre-heat treatment testing, to ensure that surface effects did not influence the results. After heat treatment and surface preparation the thickness of the samples was measured to ensure that there would be minimal sample thickness effects

on the EM signal (i.e. the skin depth at the test frequency of the EM signal was less than the sample thickness). The measured sample thickness (measured using callipers with accuracy of ±0.03 mm) and the calculated skin depth at 100 Hz, measured using equation 2.15 and reported permeability and resistivity values for the steels of interest, are given in Table 3.3. It can be seen from Table 3.3 that the thickness values of the three samples are greater than the skin depth.

Table 3.3: Sample thickness after oxidation heat treatment and surface preparation. Electromagnetic properties of the Plain Carbon Steel, P91 and T22 Grade Steel [7, 36]. Skin depth for the EM signal at 100 Hz calculated from equation 2.15.

Samples	**Thickness (mm)**	**Electrical Resistivity (μ Ω m)**	**Relative permeability (no unit)**	**Skin depth, mm**
Plain Carbon Steel	5.1±0.2	0.197±0.2	≈ 90	2.35
P91	10.3±0.2	0.240±0.2	≈ 60	3.18
T22	3.9±0.1	0.104±0.2	≈ 75	1.87

3.6. Presence of the magnetite

The spalled oxide films taken from the Plain Carbon Steel and T22 Grade steel after heat treatment were tested using a permanent magnet to determine if magnetite was present. Magnetite is ferro-magnetic while wustite and hematite are paramagnetic, therefore if magnetite is present in the oxide film it will be attracted to the permanent magnet. There was no spalled oxide film from the P91 Grade Steel due to its high oxidation resistant and it was not possible to remove any significant amount of oxide from the samples for magnetic testing.

4. Results and Discussions

4.1.Microstructure of samples (Oxide film and steel) after heat treatments

Plain carbon steels are widely used in applications at low temperature in coal fired power plants, and the Plain Carbon (PC) steel used in this work acts as a reference sample. The T22 Grade tube is a 2.3 wt-% Cr steel and the P91 steel is a 9 wt-% Cr steel, which are both currently used in boiler tube, superheated coils and steam piping applications in coal fired power plants.

4.1.1. Microstructure and Hardness of the Plain Carbon steel, P91 and T22 Grade Steel

The microstructures of the 0.17wt% C Plain Carbon steel before and after the oxidation heat treatment at 700^0C for 75 hours are shown in figure 4.1. The microstructures consist of ferrite (white regions) and pearlite (grey regions) and there are no significant differences in appearance between the two conditions at this magnification.

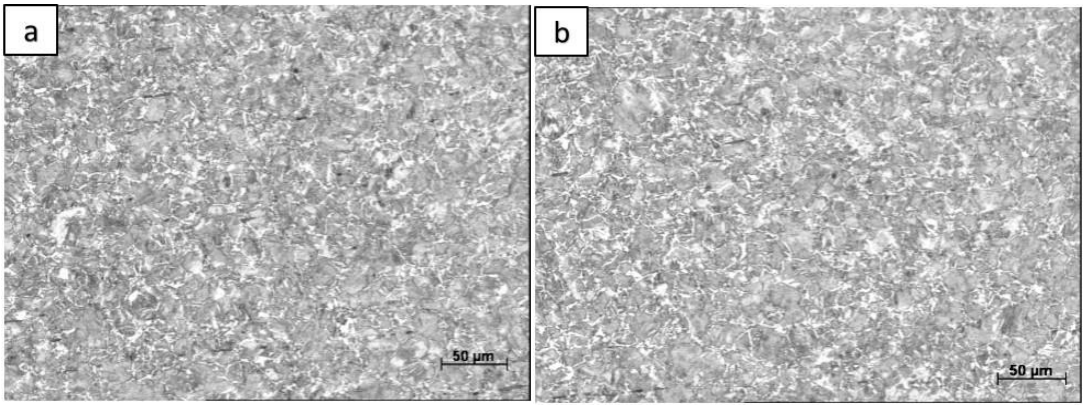

Figure 4.1: Microstructures of the Plain Carbon steel (a): before and (b): after the heat treatment at 700^0C for 75 hours.

The microstructures of the P91 grade steel before and after heat treatment at 700 ^{0}C for 75 hours are shown in figure 4.2. The microstructures in both cases are tempered martensite; it is possible that some coarsening of the martensitic laths will have resulted from the heat treatment, based on the microstructural changes reported in the literature for P9 and P91 grade steels [33].

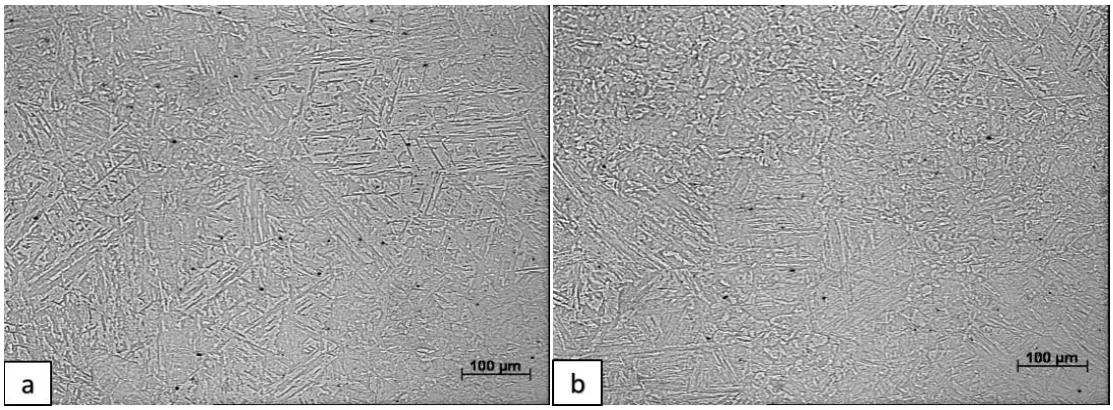

Figure 4.2: Microstructures of the P91 grade steel (a): before and (b): after the heat treatment at 700 ^{0}C for 75 hours.

The microstructures of the T22 grade steel before and after heat treatment at 700 ^{0}C for 75 hours are shown in figure 4.3. The microstructure is mixed pro-eutectoid ferrite (white) and bainite (grey).

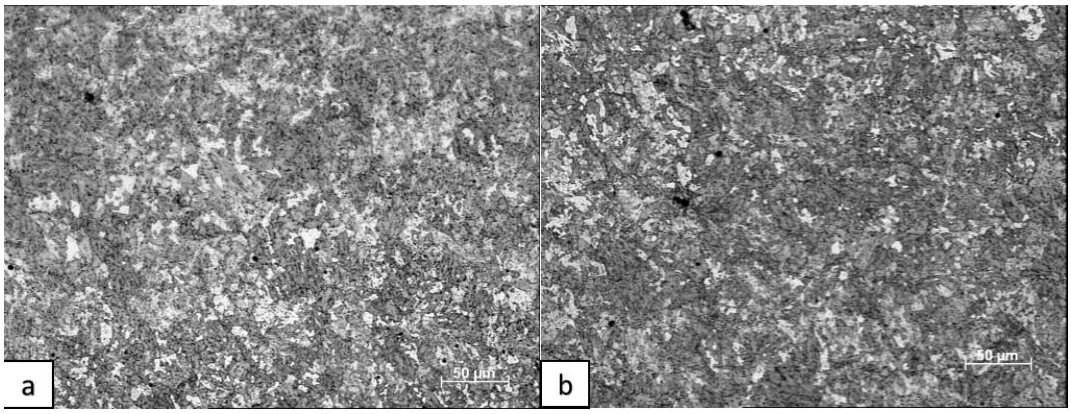

Figure 4.3: Microstructures of the T22 Grade steel (a): before and (b): after the heat treatment at 700^{0}C for 75hours

4.1.2. Hardness of the heat treated samples

The hardness measurements for the plain carbon steel samples before and after each heat treatment are given in A7.1. The mean values of hardness are plotted against heat treatment time in figure 4.4. There is a decrease in hardness from 177.5 Hv to 105.5 HV during the heat treatment process at 700 ^0C. At 650 ^0C the hardness shows a smaller drop from 177.5 Hv to 139.7 Hv (25 h to 75 h). The decrease in hardness may be due to the spheroidising the pearlitic carbides in the carbon steel, which is known to decrease the hardness of the steel [20].

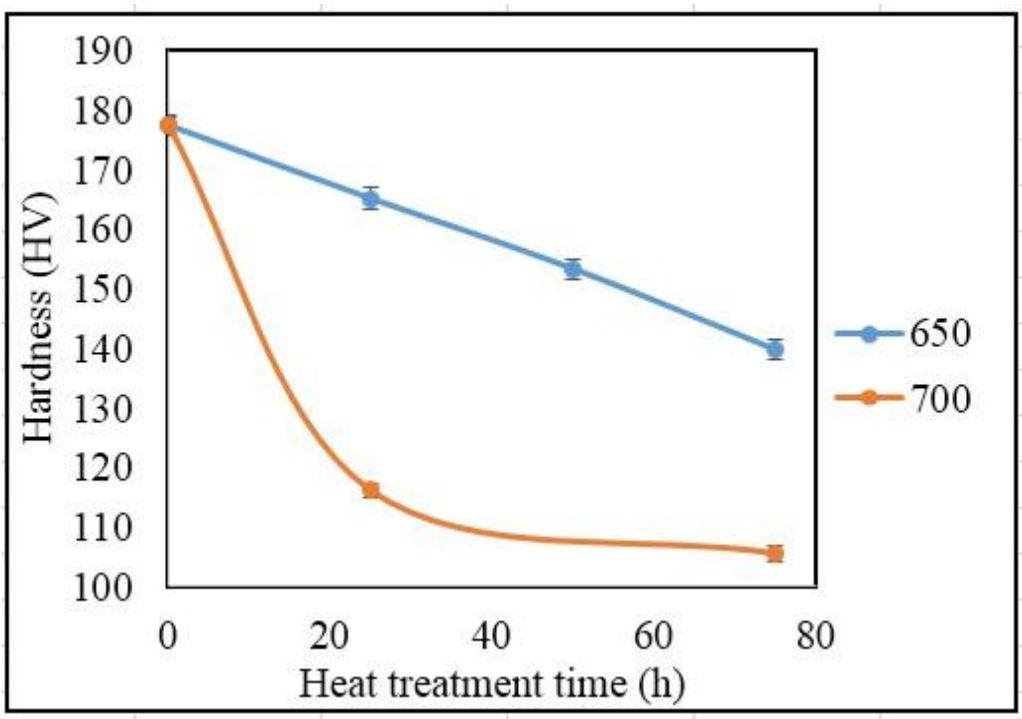

Figure 4.4: The average hardness of the Plain Carbon steel samples against heat treatment time at 650 ^0C (blue curve) and 700 ^0C (red curve)

A summary of hardness measurements for the P91 grade steel is given in A7.2. The average values are plotted against heat treatment time in figure 4.5. There is a small drop in hardness for the P91 steel during heat treatment at both 700 ^0C and 650 ^0C. This is due to the tempering process coarsening the precipitates and laths in the martensitic microstructure (P91) [34].

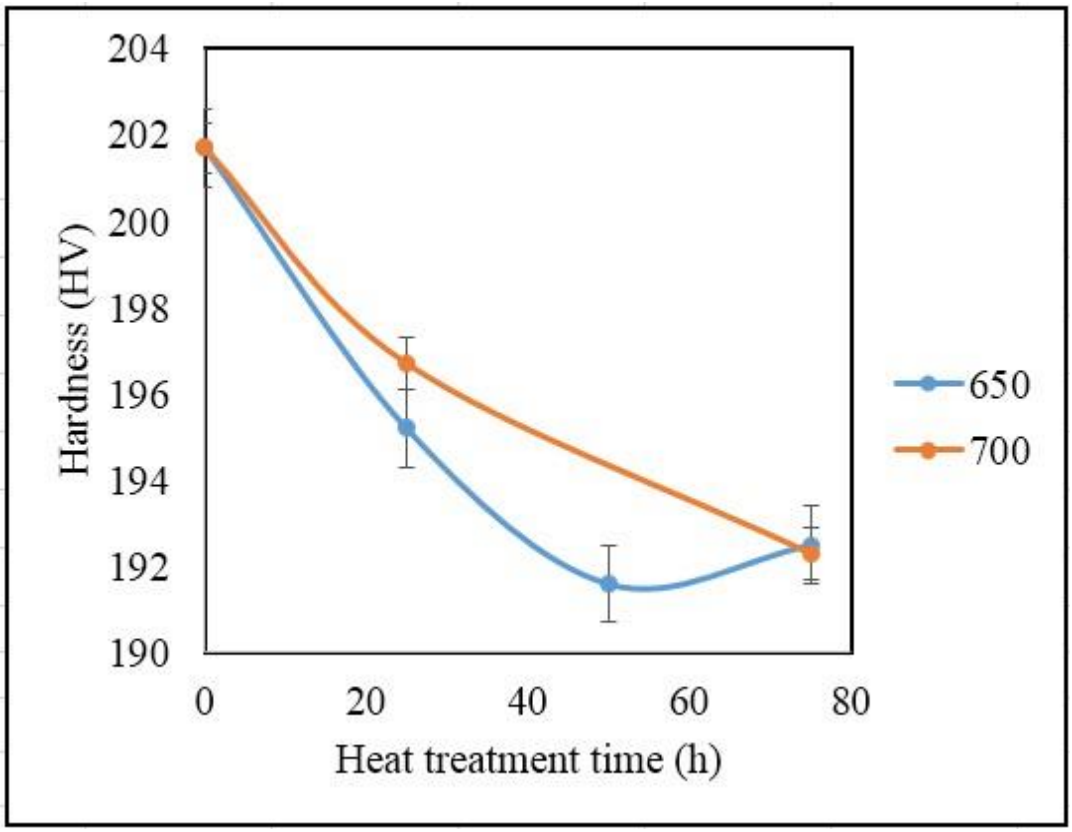

Figure 4.5: The average hardness of P91 Grade Steel Samples against oxidation time at 650 ^{0}C (blue curve) and 700 ^{0}C (red curve)

A summary of the hardness measurements for the T22 grade steel is given in A7.3. The average values are plotted against the heat treatment time in figure 4.6. The hardness values only decrease slightly after heat treatment (by approx. 8 Hv), this is as expected since the as-received material had already experienced long term thermal exposure, albeit at a lower temperature than the heat treatments (520 ℃ rather than 650 or 700 ℃), therefore only limited further tempering was expected. The drop in hardness may be due to the additional tempering process further coarsening the precipitates, which is known to decrease the hardness of the steel [34].

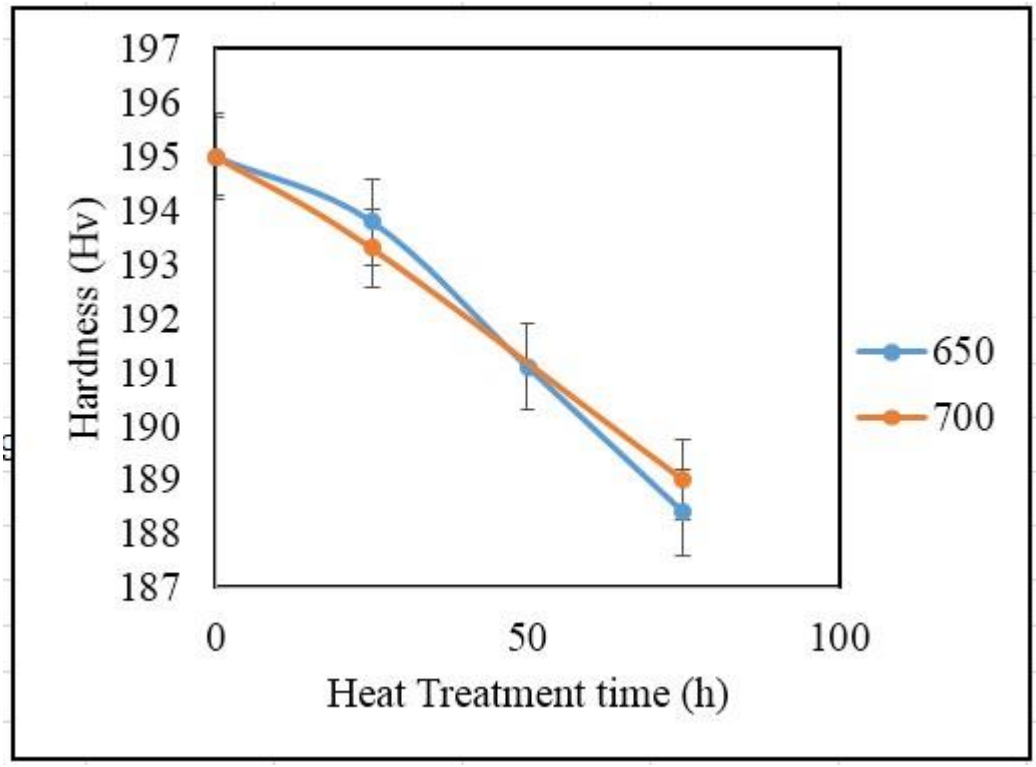

Figure 4.6: The average hardness of T22 Grade Steel Samples against oxidation time at 650 ^{0}C (blue curve) and 700 ^{0}C (red curve)

The average hardness of the plain carbon steel, T22 and P91 are plotted together in figure 4.7. It can be seen that the hardness of the plain carbon steel shows a significant drop on heat treating at 650 ℃ and an even greater decrease when heat treating at 700 ℃, while the hardness of T22 and P91 only shows a small decrease both at 650 and 700 ℃. T22 and P91 Grade steel maintain their mechanical strength after heat treatments at both 650 and 700 ℃ as these steels are alloyed martensitic steels designed for high temperature use; the alloying additions of Cr and Mo retard the tempering process [20,27,33]. However, the plain carbon steel is a structural grade that is designed for room temperature operation, the elevated temperatures will results in pearlite spheroidisation and therefore a loss in mechanical properties [20].

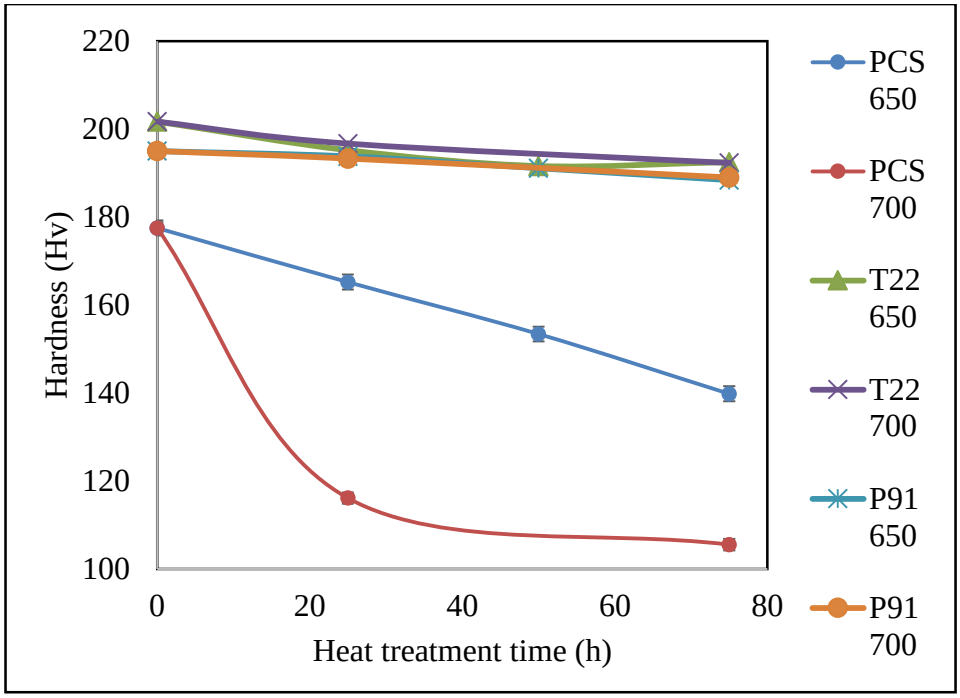

Figure 4.7: The average hardness of Plain carbon steel, T22 and P91 Grade Steel Samples against oxidation time

4.2. Oxide scale formation for the plain carbon steel, P91 and T22 Grade Steel

4.2.1. Magnetite test

The permanent magnet test results for the spalled oxide removed from the Plain Carbon Steel and T22 Grade Steel after heat treatments at different temperatures are shown in table 4.1 below. The oxide on the P91 sample did not spall off therefore could not be tested. The results are consistent with magnetite being present in the oxide layer, which is in agreement with the literature [22]. .

Table 4.1:Permanent magnet test for Plain Carbon Steel and T22 Grade Steel

Samples	**Magnetite condition**				
	650 ℃			**700 ℃**	
	25h	**50h**	**75h**	**25h**	**75h**
Plain Carbon Steel	Attached	Attached	Attached	Attached	Attached
P91	-	-	-	-	-
T22	Attached	Attached	Attached	Attached	Attached

**(The oxide of P91 did not spall)*

4.2.2. Plain carbon steel

Images of the samples before and after heat treatment are shown in figure 4.8. After 25 hours heat treatment at 700 ^{0}C the surface of the sample shows oxide spalling off in some areas. However, the majority of the oxide film is still attached to the sample as shown in figure 4.8(b). After 75 hours heat treatment at 700^{0}C, a large area of the oxide had spalled off the surface (shown in figure 4.8(c)), which meant that EM sensor testing could not be carried out as there was no area large enough for accurate measurement due to the tests having to be carried out at least 10 mm from the edge of the sample (see Chapter 3.3.1).

Figure 4.8 (d)-(f) shows selected samples after heat treatment at 650^{0}C for 25, 50 and 75 hours. The plain carbon steel shows little spallation or oxide cracking after 25 hours heat treatment, such that sufficient surface area with oxide was present for EM testing. After 50 h, there is some oxide spallation, but again sufficient area with intact oxide was present for EM testing. However, after 75 h the oxide film showed some observable spallation and cracks on the surface. This is due to the low Cr content in steel leading to the low oxidation resistance. And fast oxide growth rate will introduce pores, stresses and show different growth rate of inner and outer oxide layers in the oxide film, which leads to cracking and spallation [12]. All the EM measurements were taken from the area with the least oxide cracking. The thickness measurements were taken from the area without cracking; therefore there will be no effect of these crackings on oxide thickness data obtained and on the measurements from the EM sensor.

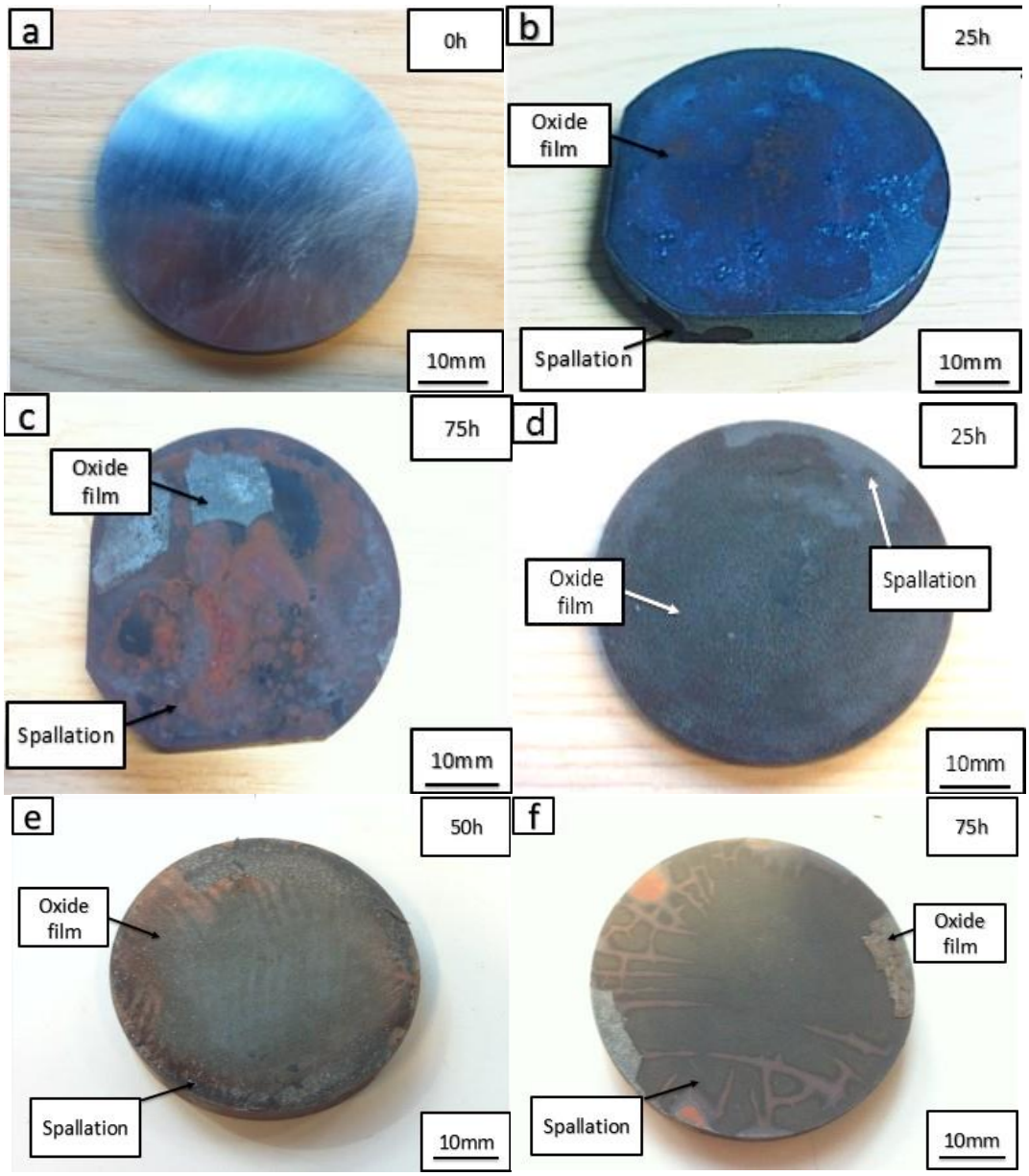

Figure 4.8: Optical images of the plain carbon steel sample after (a): 0h, (b): 25h, (c): 75h at 700^{0}C; (d): 25h, (e): 50h, (f): 75h at 650^{0}C

Optical micrographs from sectioned samples of plain carbon steel after 25 hours and 75 hours heat treatment at 650 ^{0}C are shown in figure 4.9(a) and (b) respectively. Figure 4.9(c) and (d) show plain carbon steel samples after 25 and 75 hours at 700 ^{0}C. By comparing the appearance of the oxide films with those reported in the literature, e.g. Figure 2.7, it is expected that the light area towards the bottom of the images is a mixture of hematite and magnetite, whilst the grey and black area in the middle of the images is wustite. These optical micrographs were used to measure the average oxide thickness, which is reported later.

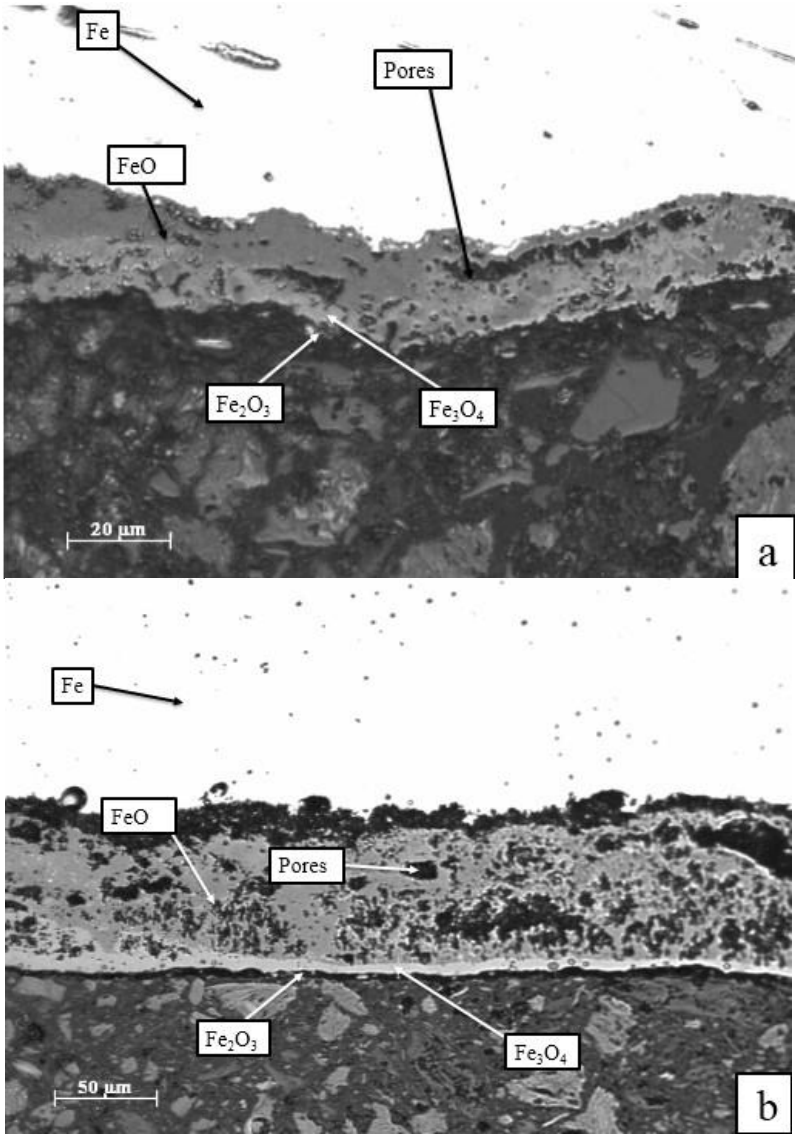
Fe
Pores
FeO
Fe_2O_3
Fe_3O_4
20 µm
a
Fe
FeO
Pores
Fe_2O_3
Fe_3O_4
50 µm
b

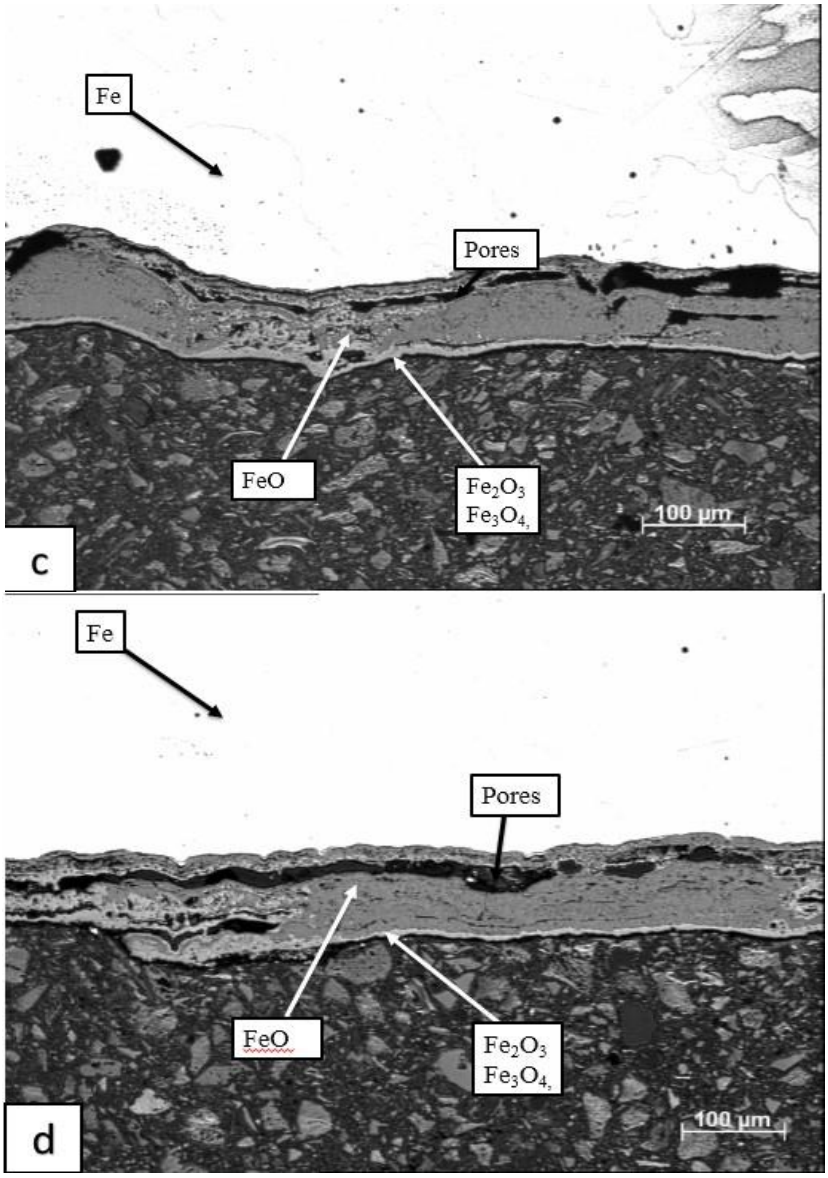

Figure 4.9: Microstructures of the oxide film formed on the plain carbon steel sample after (a): 25, (b):75 hours oxidation in the furnace at 650 ^{0}C; (c): 25, (d):75 hours oxidation in the furnace at 700 ^{0}C.

4.2.3. P91 Grade steel

Images of the samples before and after heat treatment are shown in figure 4.10. The oxide film after all heat treatments is fully adherent to the metal surface and no oxide cracks or spallation was observed. This is due to the low oxidation rate of P91 as it has a high Cr content (9 wt-%), which agrees with the literature [15].

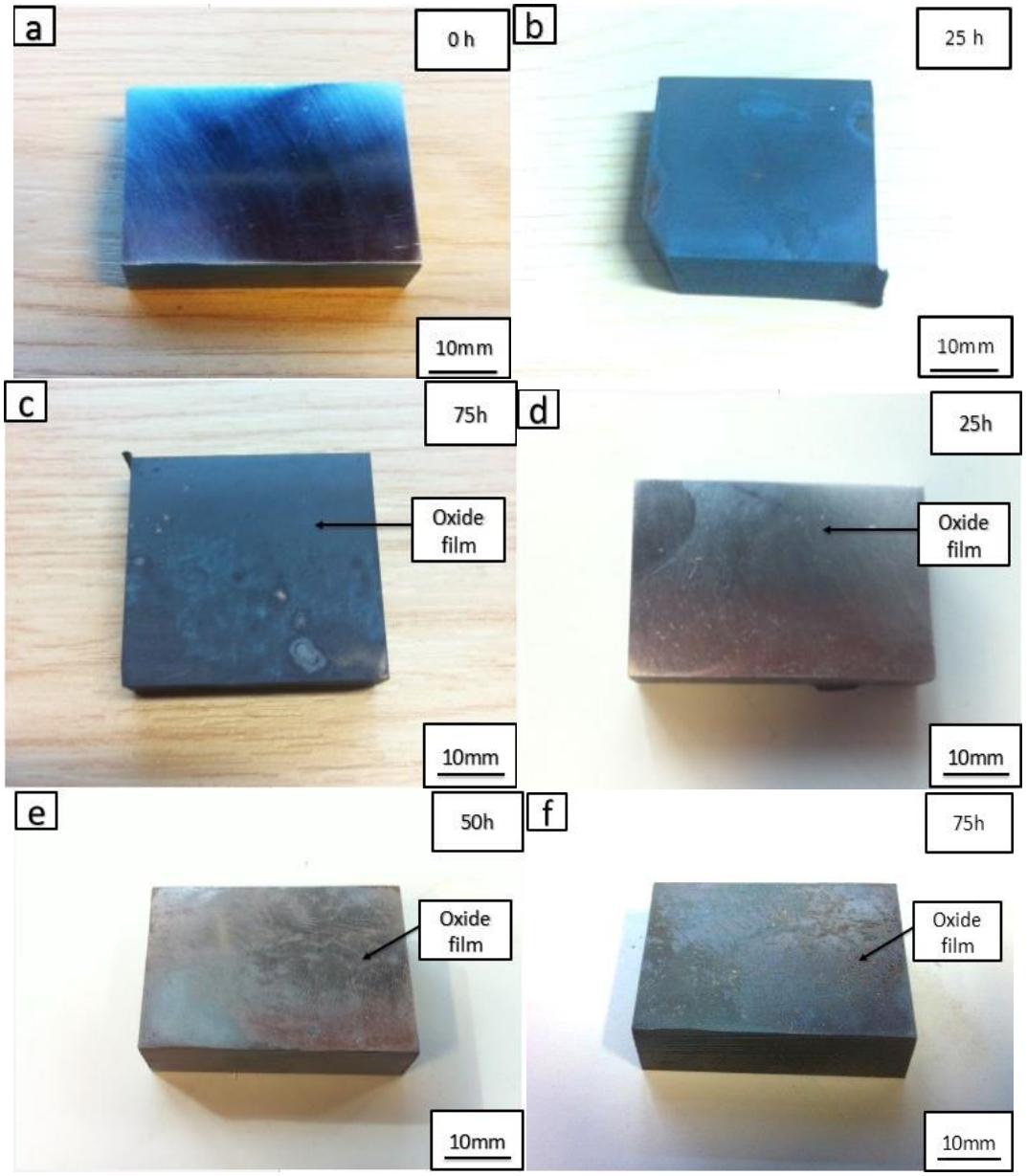

Figure 4.10: Images of the P91 steel sample before heat treatment (a) and after 25 hours (b): 75 hours at 700 ^{0}C (c): and after 25 h, (d): 50 h, (e): 75 h (f) at 650 ^{0}C

Optical micrographs of sectioned samples of P91 after 25 hours and 75 hours heat treatment at 650 ^{0}C are shown in Figure 4.11 (a) and (b) respectively. It is expected,

based on literature observations of oxide type [3], that the dark area towards the bottom of the images is a mixture of hematite and magnetite, whilst the grey and white area in the middle of the images is the inner layer of $(Fe,Cr,Mn)_3O_4$. It can be seen that the oxide film thickness in Figure 4.11 (a) is about 8.5 µm after 25 hours exposure, which increases to about 20.3 µm after 75 hours, figure 4.11 (b).

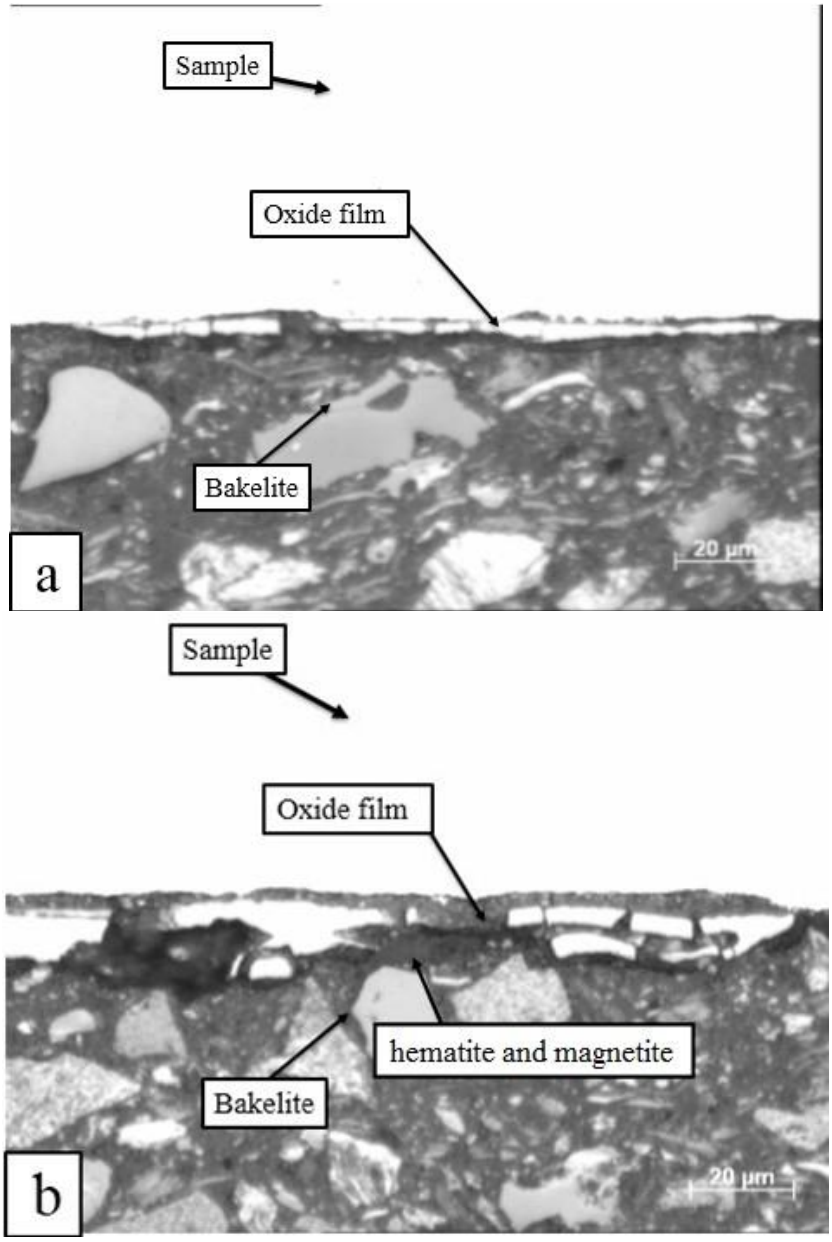

Figure 4.11: Microstructure of the oxide film formed on the P91 grade steel sample after (a): 25, (b): 75 hours oxidation in the furnace at 650 ^0C

4.2.4. T22 Grade Steel

Images of the samples before and after heat treatment are shown in figure 4.12. It can be seen from the figure that after heat treatment at 650 ℃ the oxide is fully adherent to the metal and there are no cracks present. At 700 ℃ after 25 hours there is some spalling of the oxide film at the sample edges, whilst after longer exposure (75 hours) the oxide shows cracking and there is also some loss of oxide at the sample edges. However, in all cases there is a sufficiently large area of oxide on the sample for EM testing. Therefore, it can be seen that the 2.3 wt-% Cr in T22 steel gave it a relative higher oxidation resistance than the plain carbon steel but lower than the P91 steel (9 wt-% Cr), which agrees with the literature [23, 26, 27].

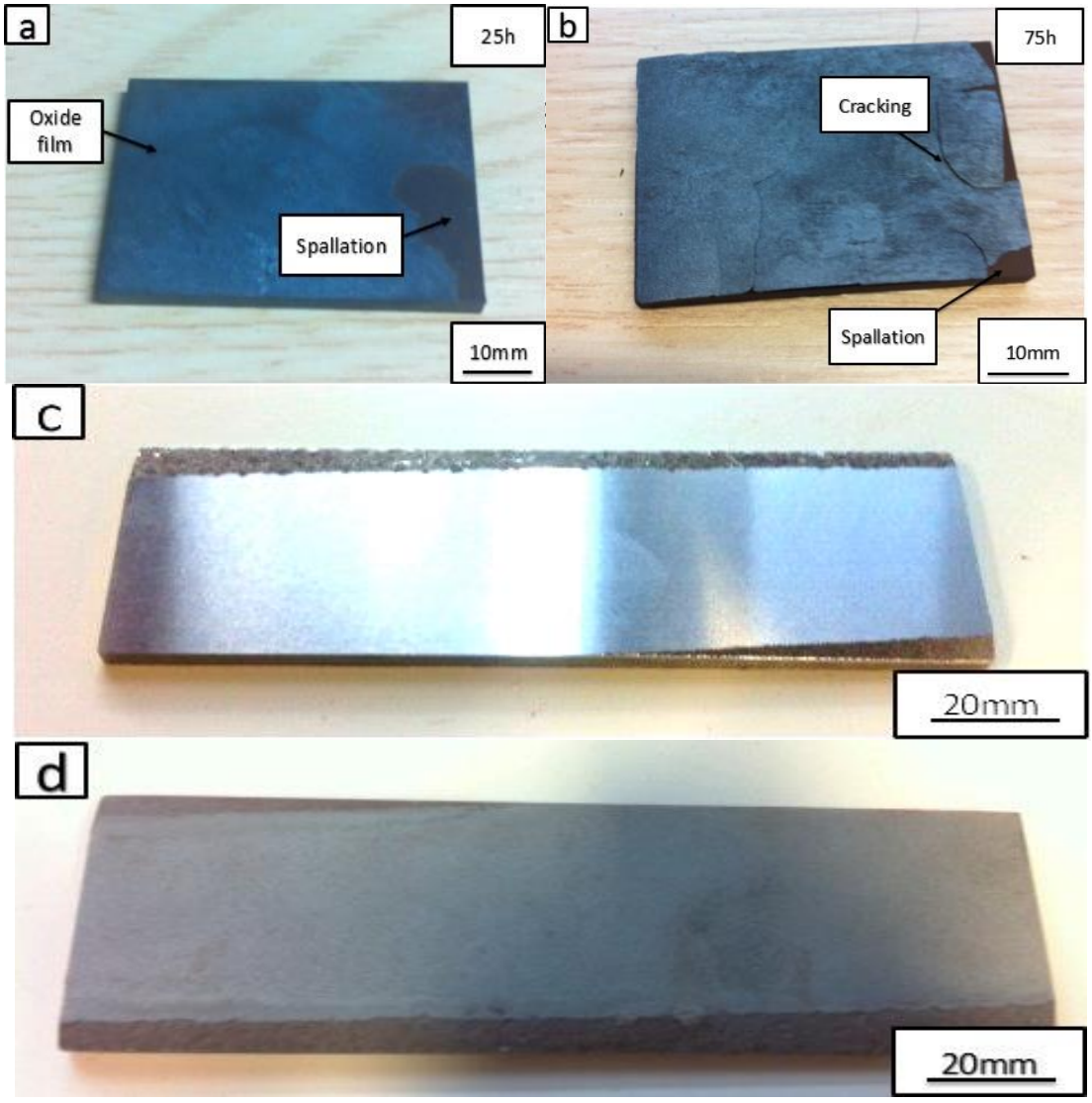

Figure 4.12: Images of the T22 steel sample after (a): 25 hours (b): 75 hours at 700 ^{0}C (c): as-received sample (d): 75 hours at 650 ^{0}C

An optical micrograph of a sectioned sample of T22 after 75 hours heat treatment at 700^0C is shown in figure 4.13. By comparing the appearance of the oxide film with that reported in the literature [24] it is expected that the white area close to the Bakelite is Fe_2O_3 (hematite), the dark area close to the bulk steel is Fe_3O_4 (magnetite) and the grey area should be mixed oxide containing Cr or wustite. The thickness of this oxide film is about 119.2 μm.

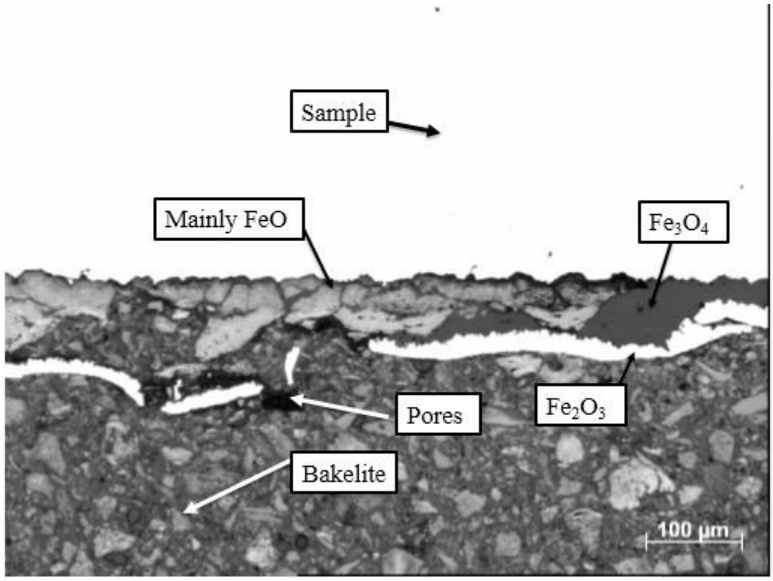

Figure 4.13: Microstructure of the oxide film formed on the T22 grade steel sample after 75 hours oxidation at 700 ^{0}C.

4.3.Overall Oxide FilmThickness

Appendix 7.4, 7.5 and 7.6 show the mean values and standard deviation values for the surface oxide thickness after the different heat treatments on the three steels investigated. Whilst there are a number of published studies on the oxidation rate and oxide thickness formed on high Cr content steels during heat treatment at 650-700 ℃ [14, 25, 29. 39] no reports on the steels compositions examined in this work have been found.

4.3.1. Plain carbon steel

It is clear shown in figure 4.14(a), that the oxide forms more rapidly at 700 ℃ compared to 650 ℃. Figure 4.14(b) shows the relationship between square of oxide thickness and time. It appears that the oxide formation at both 650 and 700 ℃ follows a parabolic growth law, which agrees with the literature [40], although as the oxide was observed to crack and spall after 75 hours a subsequent increase in growth rate may be expected. (The data given in Appendix 7.4)

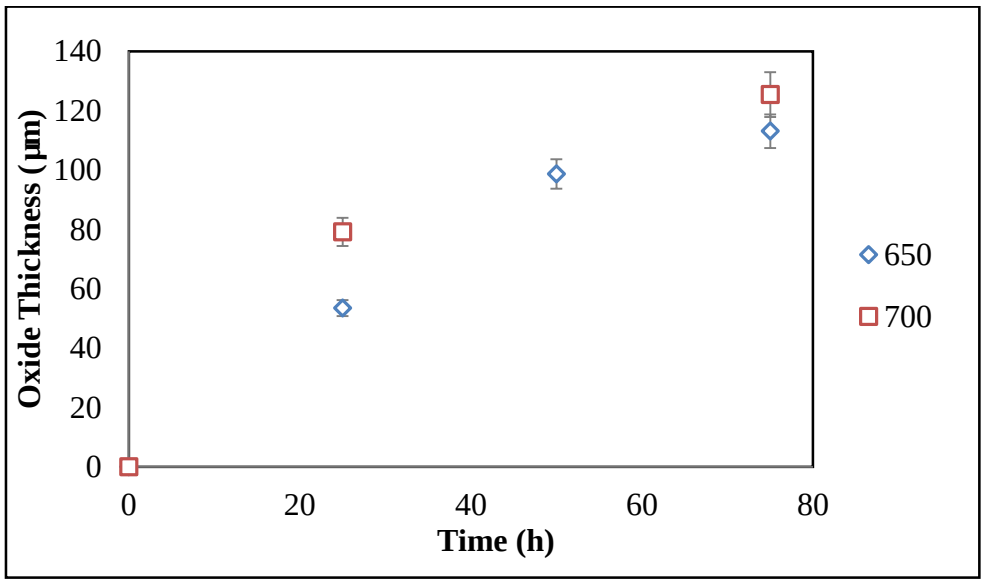

(a).

(b).

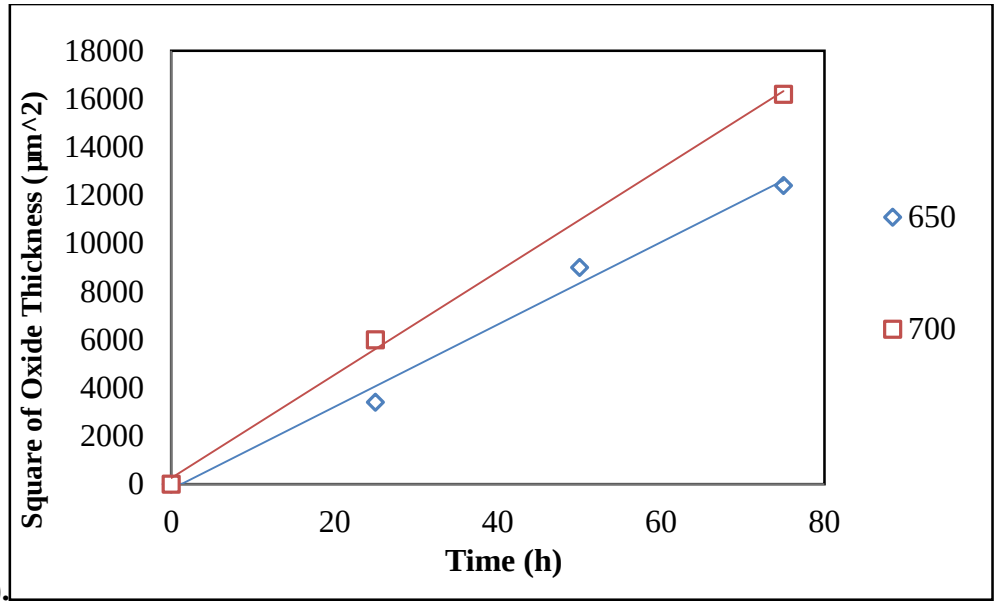

Figure 4.14: (a):Graph showing the oxide growth on the Plain Carbon Steel for durations from 0 hours to 75 hours at 650 ^{0}C (Blue Points) and 700 ^{0}C (Red Points); (b): Graph of oxide thickness squared vs time of Plain Carbon steel from 0 hours to 75 hours demonstrating parabolic behaviour at 650 ^{0}C (Blue) and 700 ^{0}C (Red)

4.3.2. P91 Grade Steel

It can be seen from figure 4.15(a) that, at 650 ^0C there was a relative slow growth rate for oxide formation, which is consistent with the high oxidation resistance reported for a higher Cr alloy (AISI410) [16]. At 700 ^0C, the initial oxide growth rate increased significantly and the oxide thickness after 75 hours was much larger than for the 650 ℃ heat treatment. Figure 4.15(b) shows that at 650 ℃, the oxide formation follows a parabolic growth law. At 700 ℃, the oxide formation does not follow the parabolic law, this may due to the spallation of the oxide [11]. (The data given in Appendix 7.5)

(a).

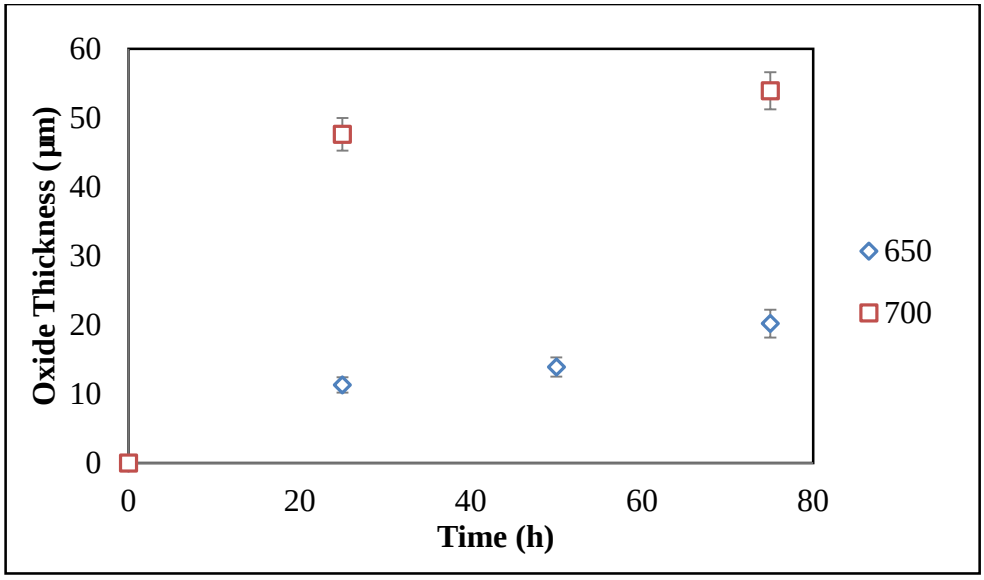

(b).

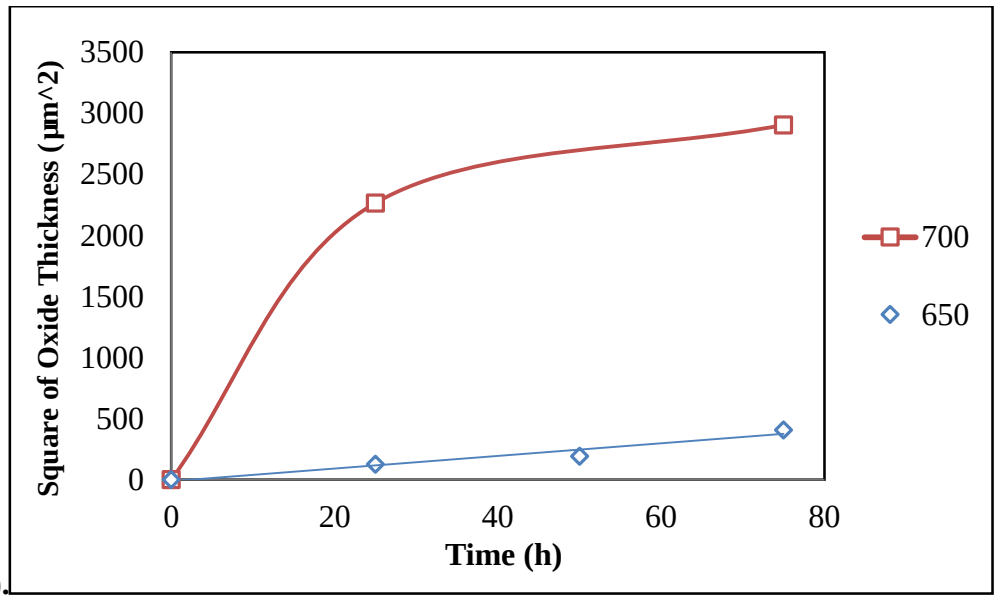

Figure 4.15: (a):Graph showing the oxide growth in P91 grade steel for durations from 0hour to 75hours at 650 ^{0}C (blue curve) and 700 ^{0}C (red curve);(b): Graph of oxide thickness squared vs time of P91 grade steel from 0 hours to 75 hours demonstrating parabolic behaviour at 650 ^{0}C (Blue Points) and not parabolic behaviour due to excessive spallation at 700 ^{0}C (Red Points)

4.3.3. T22 Grade Steel

The average oxide thickness measurements for the T22 Grade Steel samples after 25, 50 and 75 hours at 650^0C and 700^0C exposure are plotted in figure 4.16(a). The oxide thickness values under all conditions are less than for the carbon steel (which does not contain Cr) but greater than for the P91 grade steel, this is consistent with T22 material containing a lower level of Cr compared to P91 giving reduced oxidation resistance. The initial oxidation rate and oxide thickness after 75 hours heat treatment are greater at 700 ℃ than at 650 ℃. The square of average oxide thickness measurements for T22 Grade Steel samples are plotted in figure 4.16(b). It appears that the oxide formation at both 650 and 700 ℃ follows a parabolic growth law, which agree with the literature in [40]. (The data given in Appendix 7.6)

(a).

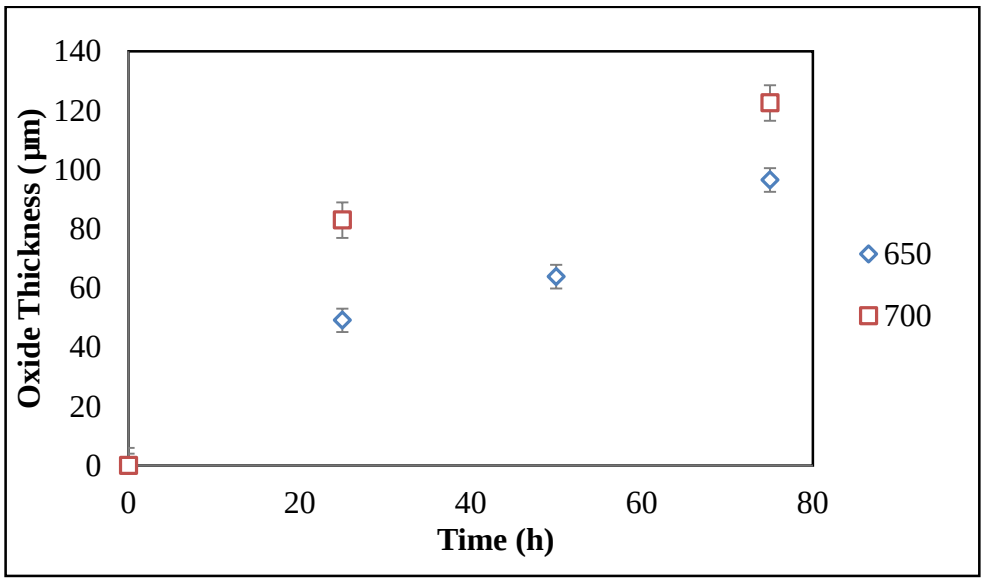

(b).

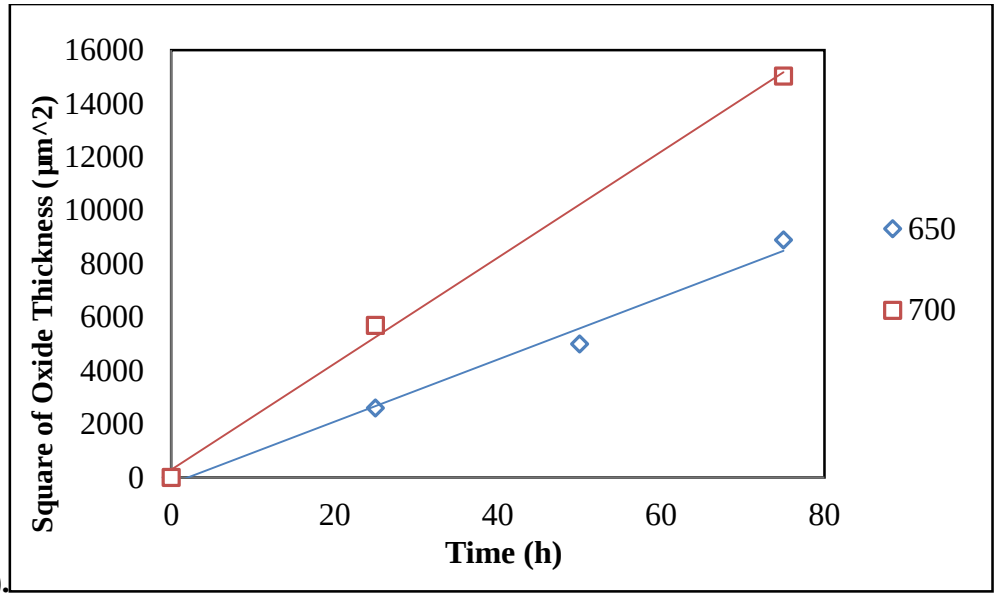

Figure 4.16: (a):Graph showing the oxide growth in T22 grade steel for durations from 0 hour to 75 hours at 650 ^{0}C (Blue) and700 ^{0}C (Red); (b): Graph of oxide thickness squared vs time of T22 grade steel from 0 hours to 75 hours demonstrating parabolic behaviour at 650 ^{0}C(Blue Points) and 700 ^{0}C (Red Points).

The square of average oxide thickness as a function of time for the Plain Carbon, P91 and T22 Grade steels are plotted in figure 4.17. It can be seen that at 650 ℃, T22 Grade steel shows much slower oxide formation than the Plain Carbon steel. When the temperature increases to 700 ℃, the oxide formation in the Plain Carbon steel is a little higher than the T22 Grade steel. T22 Grade steel is designed for high temperature use, e.g. in power plant applications, therefore it would be expected that its oxidation behaviour will be better than that of the Plain Carbon steel, however as the design operating temperatures for T22 are below 600 ℃ [2, 25], the oxidation performance deteriorates at higher temperatures and becomes more similar to the Plain Carbon steel at 700 ℃. P91 Grade Steel shows much slower oxide formation than the T22 and Plain Carbon steels both at 650 ℃ and 700 ℃. This is due to the high Cr content (9.3 wt%) in P91which improves its oxide resistance [3,9]. P91 is designed to be used at higher operating temperatures than T22 Grade steel, hence the improved oxidation resistance. P91 appears to form a relatively stable oxide film as little oxide growth is seen after 25 hours at 700 ℃ and very little oxide growth occurs at 650 ℃. It also can be seen from figure 4.17 that these heat treatments give a range of oxide thicknesses over which to test the EM instrument.

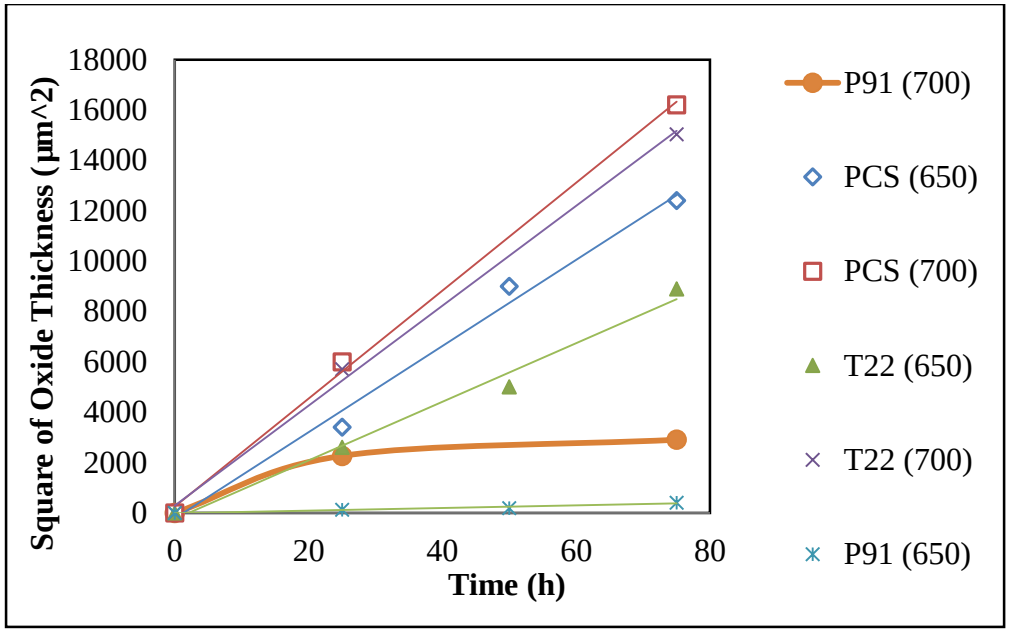

Figure 4.17: Graph of oxide thickness squared vs time of Plain Carbon, P91 and T22 Grade Steel

4.3.4. Oxide porosity measurements

The oxide porosity measurements (mean values and standard deviations) for the three steels after heat treatment for 75 hours at 650 and 700^0C are shown in table 4.2. It can be seen that the plain carbon steel oxide layer showed a relative high porosity whilst the oxide on the P91/T22 Grade steel has lower porosity. This is due to the poor oxidation resistance resulting in high oxide growth rate in plain carbon steels [8].

Table 4.2: Porosity of samples after 75 hours at 650 and 700^0C exposure

Samples	**75h 650^0C Porosity (%)**	**75h 700^0C Porosity (%)**
Low Carbon Steel	33.9 ± 4.2	38.2 ± 5.4
P91	0	4.7 ± 1.2
T22	9.6 ± 3.0	13.5± 7.6

4.4.EM signal for the lift-off effect

The measured results of the real inductance at a fixed frequency (100Hz) for Plain carbon, P91 and T22 Grade Steel samples using the EM sensor are plotted in figure 4.18 for nominal lift-off, d_x, and values of 0 – 1.04 mm, where it can be seen that the relationship between the reciprocal of the square of lift-off $(d_0 + d_x)$ and real inductance *(H)* is linear, as expected from electromagnetic theory [37]. (The data given in Appendix 7.7, 7.8 and 7.9)

It can be seen that when the EM sensor is placed directly on the sample (d_x=0), the real inductance for the three samples shows a clear difference due to the different samples' properties (relative permeability and electrical conductivity). With increasing lift-off (d_x increases; $\frac{1}{(d_0+d_x)^2}$ decreases), the real inductance values show less difference, eventually converging in value, which means that the EM sensor becomes insensitive to the different materials. Therefore, the presence of an oxide film may be important to any EM testing as it will give an increase in effective lift off as well as potentially affecting the signal due to having a magnetic character (if magnetite is present), which will be discussed in the following sections.

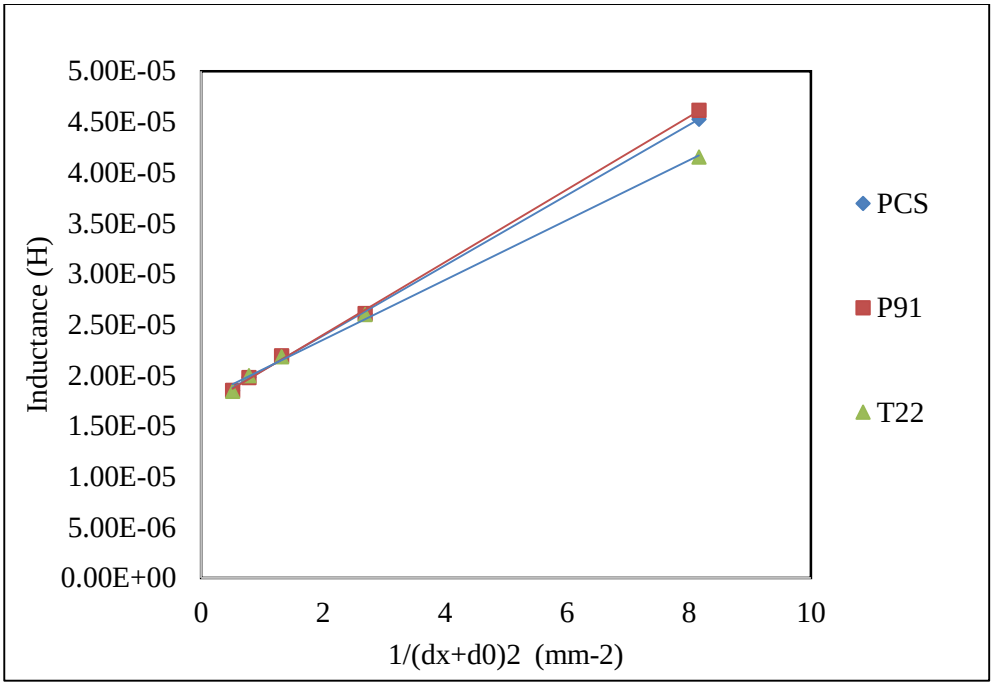

Figure 4.18: The real inductance (H) as a function of $\frac{1}{(d_x + d_0)^2}$ *in the plain carbon, P91 and T22 Grade Steels.*

4.5.EM signals for heat treated samples

4.5.1. EM signals after heat treatment (without oxide)

Table 4.3 shows that the real inductance values at 100Hz for the three steels (after the oxide was removed) after 75 hours' duration at 650^0C and 700^0C exposure. These tests were carried out to determine if the heat treatment altered the base metal inductance values. It can be seen that there are no apparent differences in the real inductance for the Plain Carbon steel and T22 steel after the heat treatments when the oxide films are removed, despite the fact that the hardness values were affected, Appendix 7.1-7.3. However, the change in inductance values for the P91 steel, as given, is greater than the experimental scatter, although the change is small compared to that seen for small changes in lift off (Appendix 7.8). The reason that the real inductance values have not changed significantly is related to the fact that the microstructures of these samples did not change a lot significantly according to figure 4.1-4.3, and it is known that the microstructural changes in steel influence the real inductance values, according to the literature [7]. It should be noted that the low frequency inductance values are reported to be related to the relative permeability of the materials [7], which are ≈90 for the Plain carbon steel, ≈75 for T22 and ≈60 for P91 (see Table 3.3). However the results in Table 4.3 do not show the expected relationship (for example P91, with the lowest relative permeability, has the highest low frequency inductance value), it is believed that this is due to the different thicknesses of the samples used in the experiments (due to limitations in the material available). In Table 3.3 it was reported that the sample thickness is greater than the skin depth expected (based on the material conductivity and relative permeability) when testing at 100Hz, however, the difference between the skin depth and sample thickness is only approx. twice for the plain carbon and T22 steels. The fact that these samples show lower inductance values that the P91 steel, Table 4.3, suggests that the sample size has affected the results. Whilst this means that the inductance values cannot be compared between the samples the trend in values during heat treatment can still be compared.

Table 4.3: The real inductance after 75 hours duration at 650^{0}C and 700^{0}C exposure at 100Hz without oxide films

Samples	**The real inductance As-received (at 100Hz) (H)**	**The real inductance 75h at 650^{0}C (at 100Hz) (H)**	**The real inductance 75h at 700^{0}C (at 100Hz) (H)**
Plain Carbon Steel	4.53E-05 ± 0.02E-05	4.55E-05 ± 0.01E-05	4.55E-05 ± 0.01E-05
P91	4.61E-05 ± 0.01E-05	4.63E-05 ± 0.01E-05	4.67E-05 ± 0.01E-05
T22	4.15E-05 ± 0.01E-05	4.15E-05 ± 0.01E-05	4.17E-05 ± 0.01E-05

4.5.2. EM signals after heat treatment (with oxide)

The average results of the real inductance versus changing frequency for the plain carbon steel samples after heat treatment at 650 ^{0}C exposure are shown in figure 4.19. At low frequency (10-100Hz), with increasing duration from 0h to 75 h, the real inductance decreases by 24.4%. At higher frequency (>10000Hz), the real inductance values for the samples decrease in a similar shape, related to the formation of eddy current in the sample reducing the inductance value [30-32]. The curve for the sample without oxide shows a steeper gradient than those for the samples with oxide, this may be due to the difference in electrical conductivity of the samples; the strength of the eddy current effect is influenced by the electrical conductivity, which will be lower for samples with an oxide film.

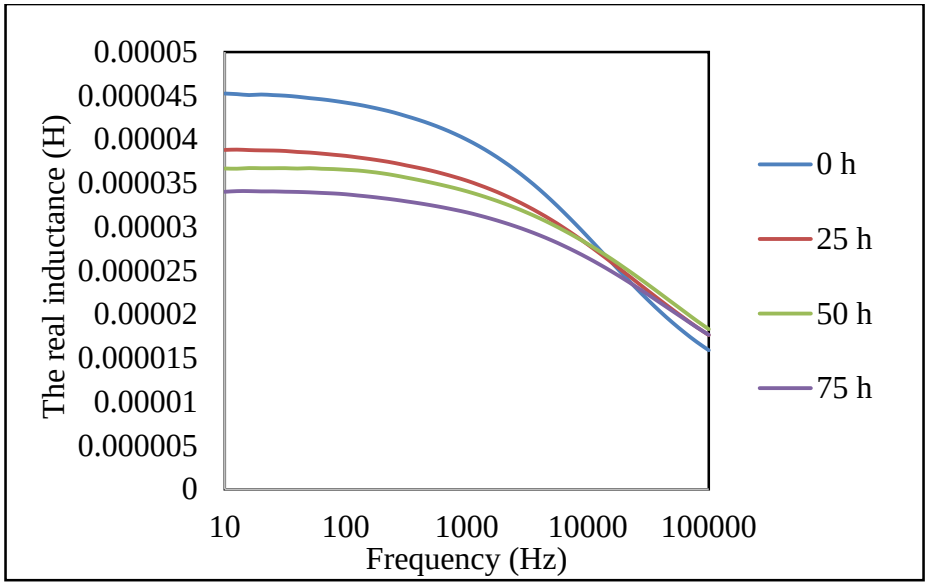

Figure 4.19: Real inductance vs. frequency for the plain carbon steel after 0, 25, 50 and 75h at 650^0C exposure

The average results of the real inductance versus changing frequency for plain carbon steel samples after selected duration at 700^0C exposure has been monitored and shown in figure 4.20. At low frequency (10-100Hz), with increasing duration from 0h to 75h, the real inductance decreases by 25.6%. With increasing frequency, the curve for the sample without oxide shows steeper gradient than those for the samples with oxide.

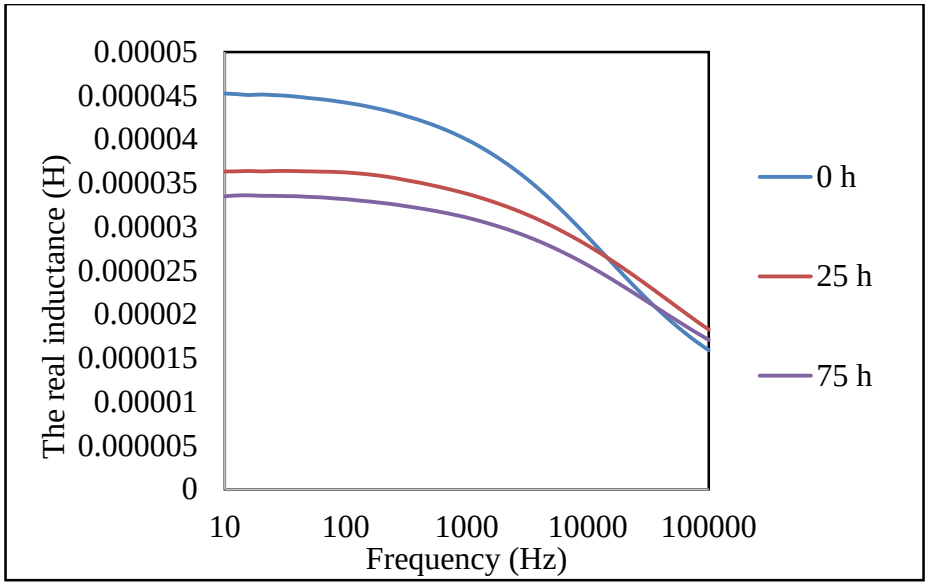

Figure 4.20: Real inductance vs. frequency for plain carbon steel after 0, 25 and 75h at 700^{0}C exposure

The average results of the real inductance versus changing frequency for P91 Grade Steel samples after selected duration at 650^{0}C exposure has been monitored and shown in figure 4.21. At low frequency (10-100Hz), with increasing duration from 0h to 75h, the real inductance decreases by 5.6%. With frequency increasing, the curve for the sample without oxide shows steeper gradient than those for the samples with oxide.

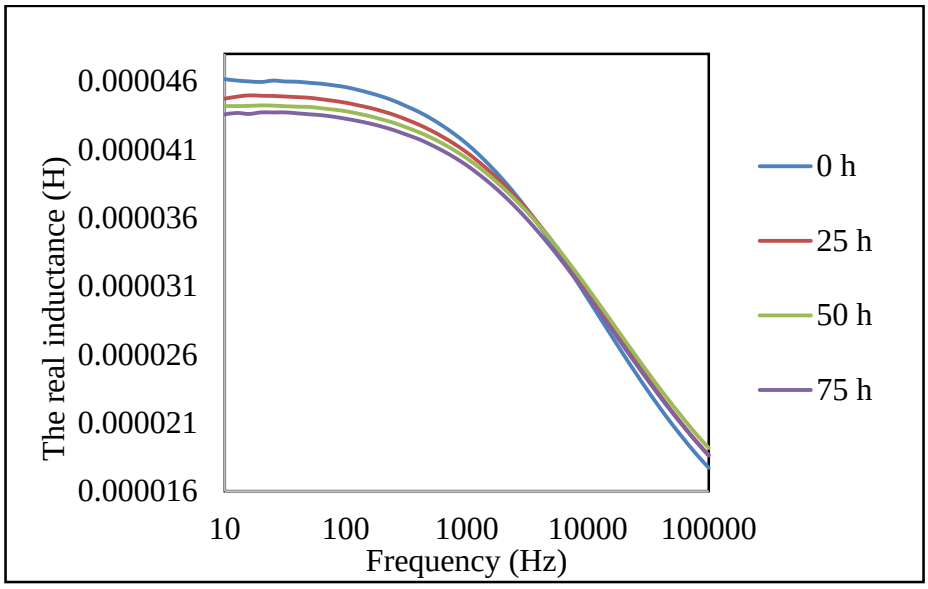

Figure 4.21: Real inductance vs. frequency for P91 Grade steel after 0, 25 and 75h at 650^{0}C exposure

The average results of the real inductance versus changing frequency for P91 Grade steel samples after selected duration at 700^0C exposure has been monitored and shown in figure 4.22. At low frequency (10-100Hz), with increasing duration from 0h to 75h, the real inductance decreases by 13.6%. With increasing frequency, the curve for the sample without oxide shows steeper gradient than those for the samples with oxide.

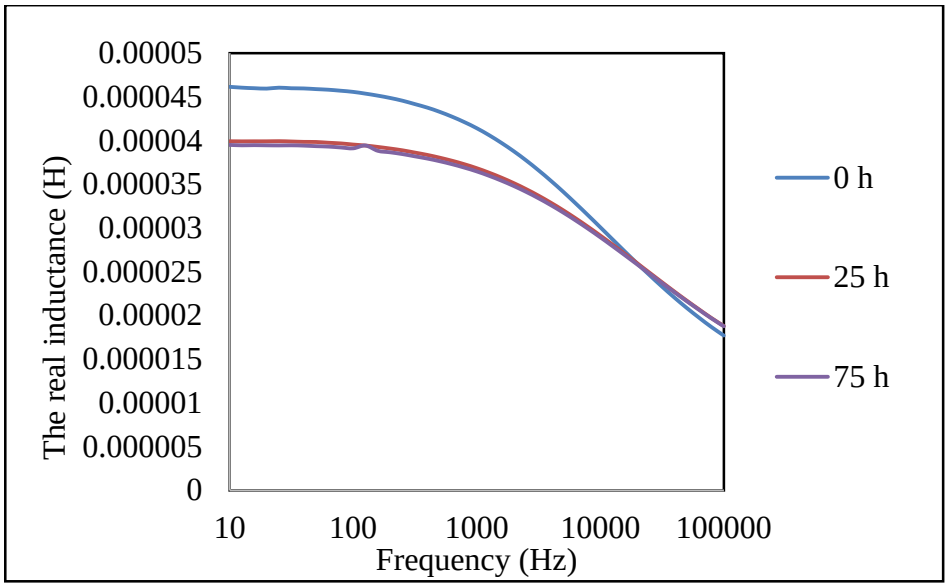

Figure 4.22: Real inductance vs. frequency for P91 Grade steel after 0, 25 and 75h at 700^0C exposure

The average results of the real inductance versus changing frequency for T22 Grade samples after selected duration at 650^0C exposure has been monitored and shown in figure 4.23. At low frequency (10-100Hz), with increasing duration from 0h to 75h, the real inductance decreases by 20.7%. At higher frequency (>10000Hz), the curve for the sample without oxide shows steeper gradient than those for the samples with oxide.

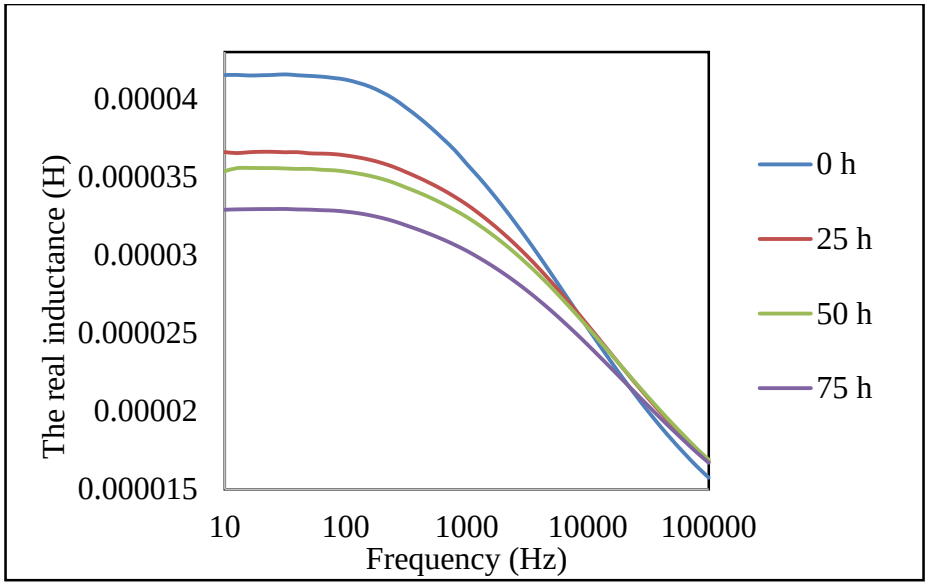

Figure 4.23: Real inductance vs. frequency for T22 Grade steel after 0, 25 and 75h at 650^{0}C exposure

The average results of the real inductance versus changing frequency for T22 Grade steel samples after selected duration at 700^{0}C exposure has been monitored and shown in figure 4.24. At low frequency (10-100Hz), with increasing duration from 0h to 75h, the real inductance decreases by 24.4%. With increasing frequency, the curve for the sample without oxide shows steeper gradient than those for the samples with oxide.

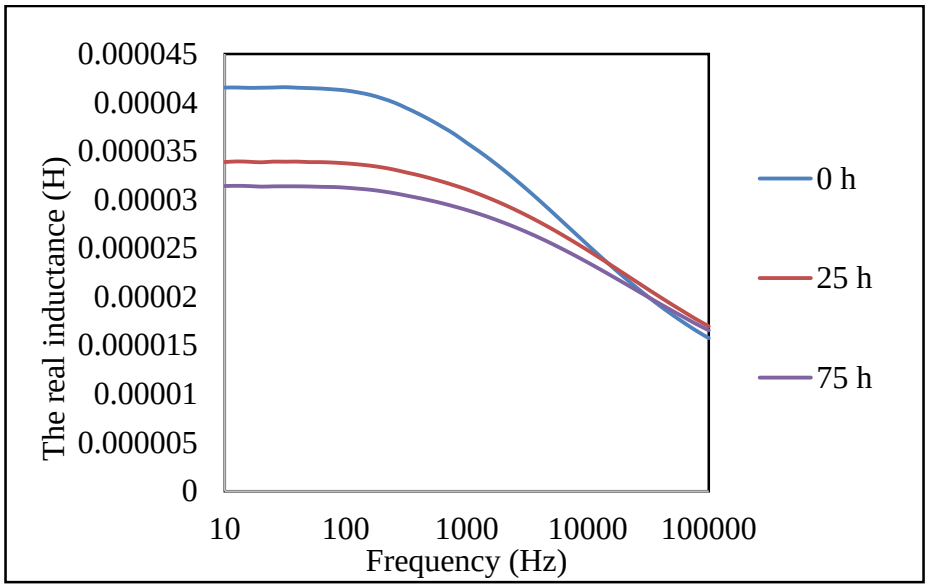

Figure 4.24: Real inductance vs. frequency for T22 Grade steel after 0, 25 and 75h at 700^{0}C exposure

At low frequency, the real inductance values are mainly influenced by the relative permeability of the samples, as discussed in section 2.2. It can be seen in figure 4.20-25 that the inductance values for the samples after heat treatments are less than the samples without any heat treatments. With increasing oxidation time, the real inductance values decreases. This is due to the relative permeability values of the oxide films formed on the samples generally being much lower than the relative permeability of plain carbon, P91 and T22 steels (Table 2.1). Whilst the relative permeability value for magnetite is higher than for the steels investigated the amount of magnetite in the oxide films formed is small (estimated to be less than 5 % according to the calculation). In addition the high porosity value for the plain carbon steel oxide film will also decrease the relative permeability as air has a relative permeability of one. Therefore the expected overall lower effective permeability of the oxide film will decrease the real inductance value measured by the EM sensor, and with an increase in the oxide films thickness, the greater the decrease in the real inductance value.

When the frequency increases, the real inductance of all the samples drops due to the eddy currents beginning to dominate the EM signals, as discussed in section 2.2. It can be seen in figures 4.19-24 that the inductance values for the samples with oxide films decrease less rapidly (with increasing frequency) compared to the samples without any oxide. When the frequency is high, the eddy currents are influenced by the electrical resistivity of the sample near the surface. The samples with oxide films have much higher electrical resistivity near the surface (Table 2.1), which can be expected to decrease the eddy current effect.

4.5.3. Real inductance vs. oxide film thickness

The real inductance values of the plain carbon, P91 and T22 (at 100 Hz) samples have been plotted against the measured oxide thickness values in figures 4.25. The standard deviations values for the real inductance measurements are small, so they are not plotted in the figures. For the plain carbon steel, the real inductance decreases by 25.6% with increasing oxide film thickness from 0 to 125.4 μm. The real inductance

decreases by 13.6% with increasing oxide film thickness from 0 to 53.9 µm for P91 steels. The real inductance of T22 steel decreases by 24.4% with increasing oxide film thickness from 0 to 122.6 µm. Therefore, with increasing of oxide thickness, the real inductance for Plain carbon steel, P91 and T22 Grade steels will decrease.

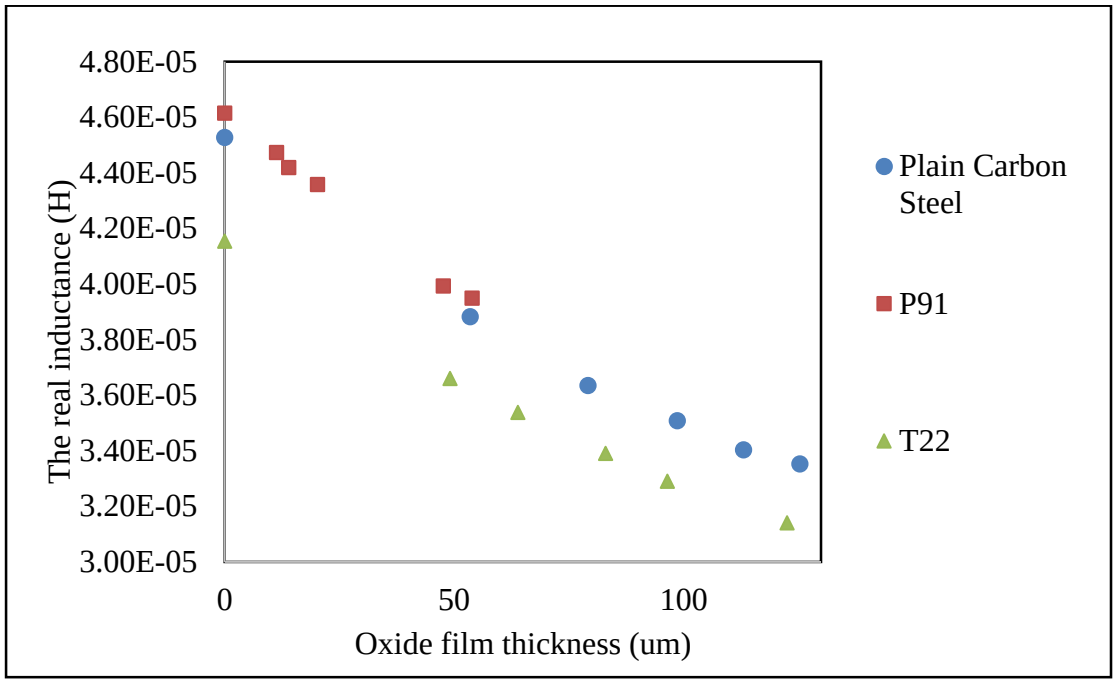

Figure 4.25: Real inductance vs. oxide film thickness at 100Hz frequency for plain carbon steel, P91and T22 Grade steel.

4.5.4. The relationship between the EM signal and the oxide film thickness and lift-off

As discussed previously the oxide film can be comprised of paramagnetic and ferromagnetic components. In order to determine how the oxide film influences the EM sensor signal the inductance values at 100 Hz for the samples with known oxide film thicknesses have been compared to the inductance values determined for an equivalent lift off value (discussed in section 4.4 in figures 4.18). It can be seen that the relationship between the reciprocal of the square of the oxide film thickness (i.e. considered as an effective "lift-off" value) ($d_{film} + d_0$) and real inductance *(H)* is linear and the data fits well with the trend line from figures 4.18 for the lift off only values. From figures 4.26-28 it can be seen that if the lift-off values (d_x) are

substituted by the oxide thicknesses (d_{Film}) of the samples, the relationship between the reciprocal of the square of lift-off ($d_{Film} + d_0$) (d_0 =0.35mm) and real inductance *(H)* is still linear. All the EM signals followed the same linear trend but show a slightly higher value than the trend in the lift-off test, this is believed to be due to an effect of the magnetite present (albeit a very small effect) and its high permeability (200) (Table 2.1).

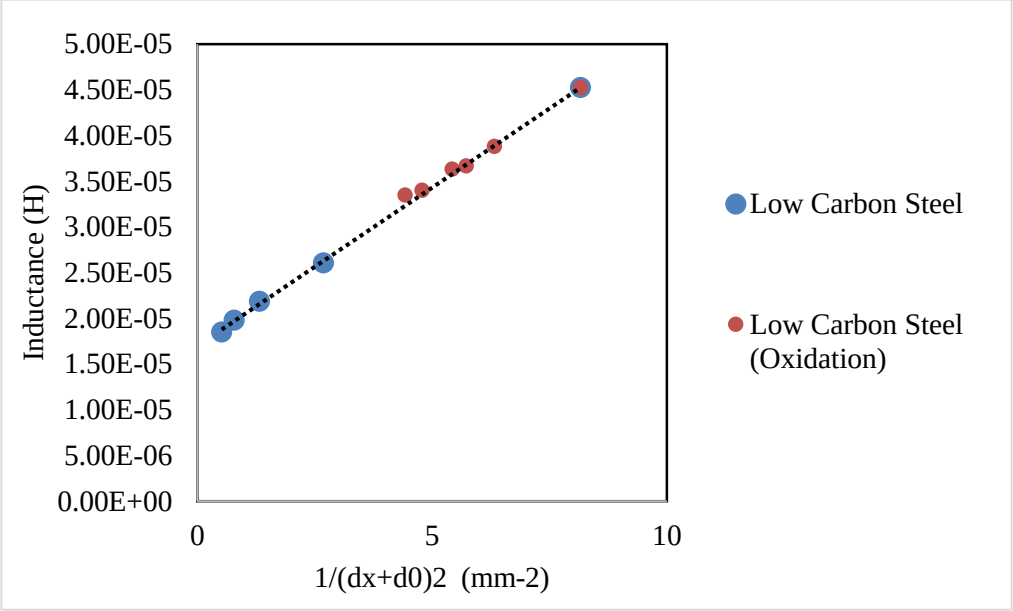

Figure 4.26: The real inductance (H) as a function of $\frac{1}{(d_x + d_0)^2}$ *(blue) and* $\frac{1}{(d_{film} + d_0)^2}$ *(red) in low carbon steel*

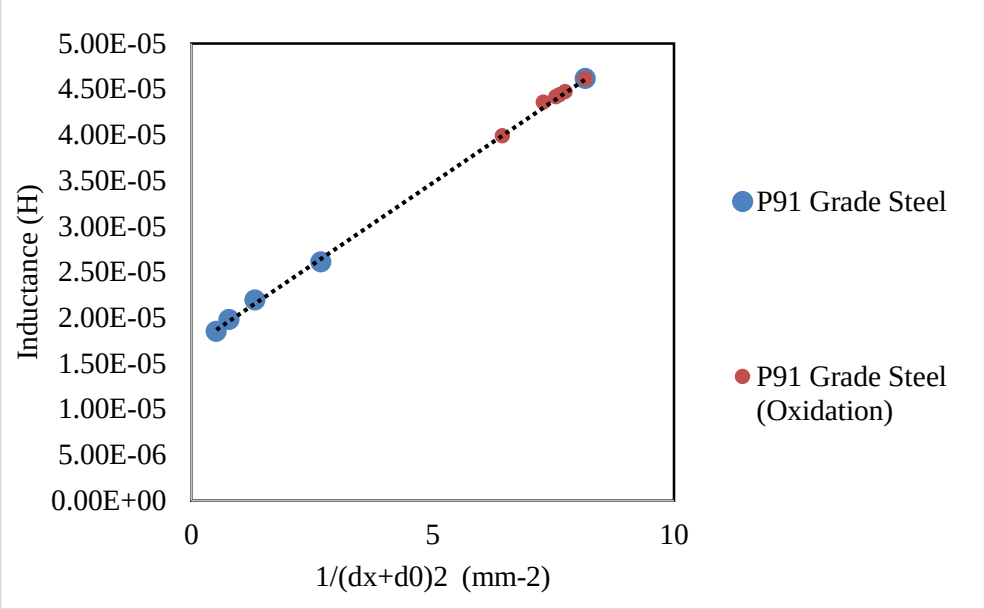

Figure 4.27: The real inductance (H) as a function of $\frac{1}{(d_x + d_0)^2}$ *(blue) and* $\frac{1}{(d_{film} + d_0)^2}$ *(red) in P91 Grade steel*

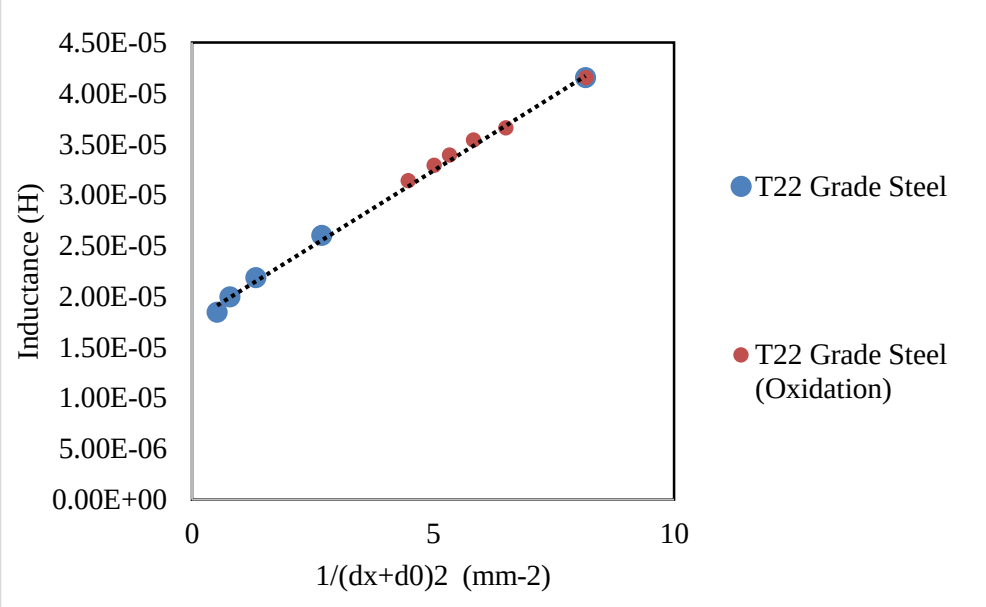

Figure 4.28: The real inductance (H) as a function of $\frac{1}{(d_x + d_0)^2}$ *(blue) and* $\frac{1}{(d_{film} + d_0)^2}$ *(red) in T22 Grade steel*

5. Conclusions and future work

5.1. Conclusions

It is known that electromagnetic (EM) sensors can be used to monitor microstructural changes in steels due to phase transformation and thermal exposure [6]. There have been no reports on how the presence of oxide films affects the EM signal. In this research three steels (one carbon steel and two power generation grade steels) have been heat treated to generate different oxide film thicknesses and the effects of the heat treatment on the EM signal have been assessed. The main conclusions from the work carried out are:

5.1.1. Oxidation behaviour

- The P91 steel shows superior oxidation resistance at both heat treatment temperatures of 650 and 700^0C due to the high (9 wt%) Cr content in this steel, which is designed for elevated temperature use in the power industry. The T22 steel shows slightly better oxidation resistance (lower rate of oxide thickness growth) than the plain carbon steel at 650^0C, due to tis Cr additions (2.3 wt%), however its oxidation resistance is similar to the plain carbon steel at 700^0C, which may be due to this temperature (700^0C) being much higher than the design temperature for operation of T22 Grade steel. It was also found that the oxide film on the plain carbon steel was more likely to spall off the surface compared to the oxide film on the P91 and T22 samples. For heat treatment at 650^0C in the range of 25 to 75 hours oxide films up to 113.1 μm thickness (20.2μm for P91 and 96.5μm for T22) were formed. As expected from the literature, the increase in Cr content in P91 compared to the T22 and the plain carbon steel resulted in improved oxidation resistance and hence thinner oxide films after heat treatment.
- The oxide films formed on the plain carbon and T22 steels contained some magnetite, which was confirmed as the spalled oxide was attracted to a permanent magnet. It is expected that the oxide on P91 contains some magnetite based on the evidence in the literature [3, 9 23], although this could not be confirmed as the

oxide film was thin and could not be removed from the sample. Significant porosity was present in the oxide films on the plain carbon steel, with smaller amounts of porosity in the oxide films on T22 and P91 steel.

- The oxidation growth rate for the plain carbon and T22 steel samples appeared to be parabolic over the heat treatment times tested. For the P91 steel under exposure at 700^0C a spallation oxide growth rate was observed.

5.1.2. EM signals

- The relationship between the reciprocal of the square of lift-off ($d_x + d_0$) (where d_x is the lift off between the sensor and sample and d_0 is the inherent lift off in the sensor where d_0 =0.35mm) and real inductance *(H)* is linear for the plain carbon steel, P91 and T22 grade steels, as expected from electromagnetic theory.
- The real inductance *(H)* value (measured at 100Hz) for the Plain carbon steels and T22 (excluding the effect of oxide film by removal of the oxide layer) show no apparent difference after heat treatments reflecting the stable nature of the microstructures to heat treatment at 650 – 700 ℃. The change in inductance values for the P91 steel, as given, is greater than the experimental scatter, although the change is small compared to that seen for small changes in lift off.
- The real inductance *(H)* value (measured at 100 Hz) decreases with increasing oxide thickness for each sample.
- The real inductance *(H)* of samples with oxide decreases less rapidly, when increasing the measurement frequency, than for the samples without any oxide. This is believed to be due to the samples with oxide films have much higher electrical resistivity near the surface (Table 2.1), which is expected to decrease the eddy current effect on the EM signal.
- When the lift-off values (d_x) are substituted by the measured oxide thickness values (d_{Film}) of the samples, the relationship between the reciprocal of the square of lift-off ($d_{Film} + d_0$) and real inductance *(H)* is still linear. All the measured EM signals for the samples with oxide followed the same trend but show a slightly higher value than for the trend in the lift-off test, which is

considered to be due to an effect of the magnetite present (albeit a very small effect).

- In summary, the effect of an oxide film on plain carbon, P91 and T22 steel on the EM sensor signal can be related to the effective lift-off from the steel to the sensor.

5.2.Future work

- The relationship between the real inductance values from EM sensor measurements and the oxide film thickness formed during heat treatment of steel samples indicates that the oxide films create an effective lift off between the sample and sensor. However, a small deviation from the lift off trend is seen, which is believed to be due to the magnetic character of the magnetite that can be present in the oxide. In order to determine the influence of any magnetite oxide, COMSOL multi-physics modelling could be used. For example, COMSOL Multiphysics 4.2a has been used previously to consider the role of microstructural pahse balance on EM sensor signals [6]. Therefore a model of a 3D H-shaped EM sensor and a steel target with an oxide layer could be used to change the properties and thickness of the oxide film, and then the relative real inductance can be calculated. The results in the model can be used as a reference to the experimental results in this report. Previously it has been found that the results from a COMSOL model fit experimental results well when considering decarburised layers on the surface of steel [6].

6. Reference

1. Osgerby, S., *Materials R&D Requirements for Fossil Fuelled Steam Plant.* In Energy Materials –Meeting the Challenge, 2008. Loughborough, UK.
2. R.Viswanathan, W.Bakker, *Materials for Ultra-Supercritical Coal Power Plants-Boiler Materials.* Part 1. Journal of Materials Engineering and Performance, 2001. 10(1): p. 81-95.
3. Ehlers, J., D.J. Young, E.J. Smaardijk, A.K. Tyagi,H.J. Penkalla, L. Singheiser, and W.J. Quadakkers, *Enhanced Oxidation of the 9%Cr Steel P91 in Water Vapour Containing Environments.* Corrosion Science, 2006. 48(11): p. 3428-3454.
4. Denny A.Jones, *Principles and Prevention of Corrosion.* 1991.: p. 304.
5. X.J. Hao, Claire.L.D., *Modelling and Measurement of Decarburisation of steels using a multi-frequency electromagnetic sensor.* Electromagnetic Nondestructive Evaluation, 2010. 31: p. 86 - 89.
6. X.J. Hao., Yin, W., Strangwood, M., Peyton, A. J., Morris, P. F. & Davis, C. L, *Modelling the electromagnetic response of two-phase steel microstructures.* NDT & E International, 2010. 43: p. 305-315.
7. Zhou, F., *1st Year PhD report. University of Bimingham.* 2011.
8. Kofstad, P., *High Temperature Oxidation of Metals.* John Wiley and Sons, Inc, 1966. New York.
9. Dogan, O.N., *Microstructural Stability and Oxidation Resistance of 9-12 Chromium Steels at Elevated Temperature.* DOE/NETL-IR-2006, 2006: p. 100.
10. Sarrazin,P., A. Galerie, and J. Fouletier,*Mechanisms of High Temperature Corros ion: A Kinetic Approach.* Switzerland: Trans Tech Publications Ltd, 2008.
11. Birks, N., G.H. Meier, and F.S. Pettit, *Introduction To The High‐Temperature Oxidation of Metals.* New York: Cambridge University Press, 2006.
12. Stott, H., G.C. Wood, and J. Stringer, *The Influence of Alloying Elements on The Development and Maintenance of Protective Scales.* Oxidation of Metals, 1995. 44(1‐2): p. 113-145.
13. Gaskell, D.R., *Introduction To The Thermodynamics of Materials 4th ed.* London: Taylor & Francis Books, Inc, 2003.

14. Fujii, *The Mechanism of The High Temperature Oxidation of Iron Chromium Alloys in Water Vapor*. Journal of the Electrochemical Society, 1964. 111(11): p. 1215-1221.
15. Fry,A., S. Osgerby, and M. Wright, *Oxidation of Alloys in Steam Environments – A Review*, NPL Report MATC(A)90, 2002.
16. Ramanathan, *Oxidation and Erosion-Oxidation Behavior of Steels.* Mat. Res., 2008. 11(1): p. 1516-1439.
17. Mannesmann, S., *DMV 304 HCu, Boiler Grade DMV 304 HCu.* in Salzgitter Mannesmann Stainless Tubes, 2008.
18. Sedriks, A.J., *Corrosion of Stainless Steels 2nd ed.* Canada: John Wiley and Sons, Inc, 1996.
19. Zurek, J., L.N. Hierro, J. Piron Abellan, L. Niewolak, L. Singheiser, W.J. Quadakkers, and p. trans tech, *Effect of alloying additions in ferritic 912%Cr steels on the temperature dependence ofthe steam oxidation resistance in 6th International Symposium on High Temperature Corrosion and Protection of Materials.* Les Embiez, France: Trans Tech Publications Ltd, 2004.
20. Callister, *Material Science and Engineering, 8th edition.* 2010: p. 430-432.
21. Francis, J.M., *Influence of minor alloying elements on structure of surface oxides formed during high temperature oxidation of an austenitic steel.* Journal of the Iron and Steel Institute, 1966. 204: p. 910.
22. F.R.Billman, *Electrochem.* 1972: p. 450.
23. Fry, S. Osgerby., M Wright, *Oxidation of Alloys in Steam Environments - A Review.* 2002. 203(89-45).
24. Saunders, M. Monteiro, and F. Rizzo, *The oxidation behaviour of metals and alloys at high temperatures in atmospheres containing water vapour: A review.* Progress in Materials Science, 2008. 53(5): p. 775-837.
25. Steve Osgerby, Tony Fry., *Simulating steam oxidation of high temperature plant under laboratory conditions: practice and interpretation of data.* Materials Research, 2004. 7(1).
26. Huczkowski, P., *Oxidation limited life times of chromia forming ferritic steels.* Materials and Corrosion, 2004. 55(11): p. 825–830.
27. Lepingle, V., G. Louis, D. Allue, B. Lefebvre, and B. Vandenberghe, *Steam oxidation resistance of new 12%Cr steels: Comparison with some other ferritic steels.* Corrosion Science, 2008. 50(4): p. 1011-1019.

28. Bozorth, R.M., *Ferromagnetism.* Van Nostrand, 1965.
29. Zhu Wenqian. Yin, Wuliang; Peyton, Anthony; Ploegaert, Henk, *Modelling and experimental study of an electromagnetic sensor with an H-shaped ferrite core used for monitoring the hot transformation of steel in an industrial environment.* NDT & E International, 2011. 44(7): p. 547-552.
30. D.C. Jiles, *Review of magnetic methods for nondestructive evaluation (Part 2).* NDT International, 1990. 23: p. 83-92.
31. X. Hao, W.Y., M. Strangwood, A. Peyton, P. Morris, C. Davis, Scripta Materialia, 2008. 58(1033-1036).
32. Graham, H.J.M., *High-Speed Signal Propagation: Advanced Black Magic*. 2003. Chapter 2(6): p. 120.
33. Zhou, H., *Final year undergraduate report, University of Birmingham.* 2012.
34. Jun.Liu, *Measurement of microstructure changes in 9Cr–1Mo and 2.25Cr–1Mo steels using an electromagnetic sensor.* Scripta Materialia, 2012. 66: p. 367–370.
35. Zheng Liu, Yehuda Kleiner, *State of the art review of inspection technologies for condition assessment of water pipes.* Measurement, 2013. 46(1-15).
36. Lefebvre, L.P., S. Pelletier, and C. Gélinas, *Effect of electrical resistivity on core losses in soft magnetic iron powder materials.* Journal of Magnetism and Magnetic Materials, 1997. 176(2–3): p. L93-L96.
37. Huang, S., Zhao, W., Zhang, Y. & Wang, S, *Study on the lift-off effect of EMAT.* Sensors and Actuators A: Physical, 2009. 153: p. 218-221.
38. K.J. Krzywosz, *On-Site Demonstration of Ferroscope Technology for Selective Leaching at R. E. Ginna Nuclear Power Plant*, IR-2008-343, December 2008
39. J. Rosser, PhD Thesis submitted, 2014
40. Juntao Yuan, Wen Wang, Shenglong Zhu, Fuhui Wang, *Comparison between the oxidation of iron in oxygen and in steam at 650-750^{0}C,* Corrosion Science, Volume 75, Pages 309-317, October 2013

7. Appendix

7.1.Hardness of heat treated samples

A 7.1: Summary of hardness measurements in Plain Carbon Steel

Samples (HT)		**Measurements (Hv)**			**Average (Hv)**	**Standard Deviation**
As received	0 h	172.7	189.5	170.3	177.5	10.5
700 ^0C	25 h	110.3	120.6	117.5	116.1	5.3
	75 h	102.2	103.5	110.8	105.5	4.6
650 ^0C	25 h	168.6	157.9	169.0	165.2	6.3
	50 h	154.3	160.6	145.2	153.4	7.7
	75 h	142.8	136.5	140.0	139.7	3.2

A 7.2: Summary of hardness measurements for the P91 grade steel.

Samples (HT)		**Measurements (Hv)**			**Average (Hv)**	**Standard Deviation**
P91	0h	200.1	195.7	209.3	201.7	6.9
700 ^0C	25h	198.4	197.2	194.5	196.7	2.0
	75h	191.1	192.9	193.0	192.3	1.1
650 ^0C	25h	199.3	193.7	192.6	195.2	3.6
	50h	191.9	192.0	190.9	191.6	0.6
	75h	193.4	194.8	189.2	192.5	2.9

A 7.3: Summary of hardness measurements in T22 Grade Steel

Samples (HT)		**Measurements (Hv)**			**Average (Hv)**	**Standard Deviation**
T22	0h	196.7	190.5	197.9	195.0	4.0
700 ^0C	25h	189.6	196.0	194.3	193.3	3.3
	75h	187.2	189.4	190.3	189.0	1.6
650 ^0C	25h	195.2	193.7	192.6	193.8	1.3
	50h	191.6	190.0	191.7	191.1	1.0
	75h	189.2	186.9	189.0	188.4	1.3

7.2.Overall oxide film thickness

A7.4: The average oxide thickness measurements (in µm) for the oxide film on the plain carbon steel samples after the different heat treatment times (25, 50 and 75 hours) at 650 ^0C and 700 ^0C.

Time(h)	Thickness 650^{0}C (*µm*)	Thickness 700^{0}C (*µm*)
25	53.5 ±7.3	79.2 ±14.6
50	98.7 ±9.2	-
75	113.1 ±8.5	125.4 ±11.0

A7.5: The average oxide thickness measurements (in μm) for the oxide film in the P91 Grade steel samples after selected duration at 650 ^{0}C and 700 ^{0}C exposure

Time(h)	Thickness 650^{0}C (*μm)*	Thickness 700^{0}C (*μm)*
25	11.3 ±1.5	47.6 ±4.8
50	13.9 ±2.2	-
75	20.2 ±6.4	53.9 ±7.1

A7.6: The average oxide thickness measurements (in μm) for the oxide film in the T22 Grade steel samples after selected duration at 650 ^{0}C and 700 ^{0}C exposure

Time(h)	Thickness 650^{0}C (*μm)*	Thickness 700^{0}C (*μm)*
25	49.1 ±7.9	83.0 ±7.8
50	63.9 ±9.8	-
75	96.5 ±13.1	122.6 ±8.7

7.3.Hardness of heat treated samples

A7.7: Summary of measurements for lift-off effects for plain carbon steel

Lift off distance *(d_x), mm*	**Inherent lift off distance within the sensor (d_0), mm**	$\frac{1}{(d_x + d_0)^2}$ **(1/mm^2)**	**Inductance *(H) at 100Hz***
0	0.35	8.163	4.526 E-05
0.26	0.35	2.687	2.607 E-05
0.52	0.35	1.321	2.187 E-05

0.78	0.35	0.783	1.981 E-05
1.04	0.35	0.518	1.849 E-05

A7.8: Summary of measurements for lift-off effects for P91 Grade Steel

Distance *(d_x), mm*	**Inherent lift off distance within the sensor (d_0), mm**	$\frac{1}{(d_x + d_0)^2}$ **(1/mm^2)**	**Inductance *(H) at 100Hz***
0	0.35	8.163	4.614 E-05
0.26	0.35	2.687	2.608 E-05
0.52	0.35	1.321	2.191 E-05
0.78	0.35	0.783	1.978 E-05
1.04	0.35	0.518	1.850 E-05

A7.9: Summary of measurements for lift-off effects for T22 Grade Steel

Distance *(d_x), mm*	**Inherent lift off distance within the sensor (d_0), mm**	$\frac{1}{(d_x + d_0)^2}$ **(1/mm^2)**	**Inductance *(H) at 100Hz***
0	0.35	8.163	4.152 E-05
0.26	0.35	2.687	2.600 E-05
0.52	0.35	1.321	2.182 E-05
0.78	0.35	0.783	1.980 E-05
1.04	0.35	0.518	1.843 E-05